

1 **Aeolian dust accretion outpaces erosion in the formation of Mediterranean**
2 **alpine soils. New evidence from the periglacial zone of Mount Olympus,**
3 **Greece**

4

5 Michael Styllas¹, Christos Pennos², Aurel Persoiu^{3,4}, Athanasios Godelitsas⁵, Lambrini Papadopoulou⁶,
6 Elina Aidona⁷, Nikolaos Kantiranis⁶, Mihai N. Ducea^{8,9}, Matthieu Ghilardi¹⁰, Francois Demory¹⁰

7

8 ¹ GEOSERVICE LTD, Eirinis 14 Street, 55236, Thessaloniki, Greece

9 ² Department of Geography, University of Bergen, Fosswinckels Gate 6, 5007, Bergen, Norway

10 ³ Emil Racoviță Institute of Speleology, Romanian Academy, Cluj-Napoca, 400006, Romania

11 ⁴ Stable Isotope Laboratory, Ștefan cel Mare University, Suceava, 720229, Romania

12 ⁵ Department of Geology and Geoenvironment, National and Kapodistrian University of Athens, Zografou
13 Campus, 15784 Athens, Greece

14 ⁶ Department of Mineralogy, Petrology and Economic Geology, School of Geology, Aristotle University of
15 Thessaloniki, Thessaloniki, 541 24, Greece

16 ⁷ Department of Geophysics, School of Geology, Aristotle University of Thessaloniki, Thessaloniki, 541 24,
17 Greece

18 ⁸ Faculty of Geology and Geophysics, University of Bucharest, Bucharest 010041, Romania

19 ⁹ Department of Geosciences, University of Arizona, Tucson, Arizona 85721, USA

20 ¹⁰ Centre Européen de Recherche et d'Enseignement de Géosciences de l'Environnement (CEREGE) - UMR 7330
21 CNRS, AMU, IRD, Collège de France, INRAE - Europôle de l'Arbois BP80 13545 Aix-en-Provence CEDEX 04 –
22 France

23

24 Corresponding author: Michael Styllas (mstyllas@gmail.com)

25

26 Note: This paper is a non-peer reviewed preprint submitted to EarthArXiv. It has been submitted to
27 Earth Surface Processes and Landforms for peer-review.

28

29

30

31 **Abstract**

32

33 Soil formation in Mediterranean periglacial landscapes remains poorly understood as the interplay
34 between erosion and aeolian dust accretion in providing parent materials, and mineral weathering
35 and pedogenesis, as dominant post depositional processes, depends on a variety of local and
36 regional factors. Herein, we investigate the balance between erosion and aeolian dust accretion in
37 the formation of an alpine soil profile along an erosional gradient in the periglacial zone of Mount
38 Olympus in Greece. We applied a wide range of analytical methods to 23 samples, from a soil profile
39 developed in a glaciokarstic plateau, from colluvial sediment horizons interbedded in postglacial
40 scree slopes and from modern Sahara dust samples deposited on the snowpack. Colluvial sediment
41 horizons exhibit high concentrations of calcite rich sand and represent the local erosion products.
42 The soil B horizon developed on a glaciokarstic plateau contains high amounts of fine earth and is
43 rich in quartz, mica, plagioclase, clays, and Fe-Ti oxides. Based on its physical and textural
44 characteristics the soil profile is partitioned in a surficial weathered Bw and a lower illuvial Bt horizon
45 that overlies the local regolith composed of fragmented glacial till and slope wash deposits.
46 Radiogenic isotope systematics, textural and mineralogical analysis show that the contribution of
47 Sahara and locally sourced dust to the development of the soil B horizon ranges between 50 and
48 65%. Cryoturbation results in fine earth translocation from Bw to the Bt horizon, whereas weak
49 pedogenetic modifications of aeolian and bedrock-derived minerals result in magnetic mineral
50 weathering and secondary clay formation. Our findings reveal that, aeolian dust accretion is the
51 dominant process in providing alpine soil parent material and that cryoturbation, weak pedogenesis,
52 and clay mineral alteration occur within the Mediterranean periglacial zone of Mount Olympus.

53

54 **Keywords:** alpine soil; erosion; aeolian dust accretion; mineral weathering; Mediterranean periglacial
55 zone, Mount Olympus

56

57

58 **1. INTRODUCTION**

59 Global glacier retreat and the melting of permafrost and ground ice have altered the dynamics of the
60 alpine critical zone by enhancing erosion and by disturbing the production of mountain soils
61 (Haeberli et al., 2006, Egli et al., 2014). During periods of glacial retreat and paraglacial adjustment,
62 alpine soils develop from parent materials sourced through a combination of frost shattering,
63 colluvial activity, and hillslope outwash (Egli and Poullenard, 2016). An equally important factor that
64 affects the formation and evolution of alpine soils is the accretion of local and long-range
65 transported aeolian dust (Muhs and Benedict, 2006; Küfmann 2008; Lawrence et al., 2013; Drewnik
66 et al., 2014; Yang et al., 2016; Gild et al., 2018; Munroe et al., 2019). Thus, the contributions of
67 physical erosion and aeolian dust accretion are fundamental sources of alpine soil parent material
68 and largely define their textural, mineralogical, and geochemical characteristics.

69 The postglacial adjustment of alpine valleys is inherently linked to high rates of erosion, with
70 frequent rockfalls, debris flows, rock avalanches, and high rates of sediment production especially
71 below steep rockwalls. In such dynamic environments, alpine soil mantles formed on the surface of
72 slope deposits are patchy, often truncated and constantly rejuvenated from rockfall material,
73 whereas the evolution of these soils alternates between progressive and regressive phases (Egli et
74 al., 2018). Similar soil mantles developed on sandy layers deposited on the surface of stratified scree
75 slopes are generally indicative of quiescent periods of slope processes and are thus concise indicators
76 of optimum climatic conditions and alpine landscape stability (Sanders et al., 2010). When the
77 regional climate shifts to a colder regime, intense freeze–thaw activity and frost cracking enhance
78 rockfall activity and result in the erosion and gradual burial of these incipient soil mantles. As
79 hillslope processes and scree slope aggradation diminish away from the alpine steep rockwalls, the
80 development of alpine soils on distal moraines, outwash plains, and glacially scoured plateaus can be
81 considered continuous (*sensu lato*). In these depositional environments, low erosional rates provide
82 ample time for pedogenetic processes such as chemical weathering, mineral alteration, elemental
83 translocation, and illuviation to occur, whereas other physical processes, such as cryoturbation

84 disturb the soil profiles. Alpine soils are an important component of high mountain ecosystems, so a
85 better understanding of the processes that drive their formation in climatically sensitive regions, like
86 the Mediterranean, is required.

87 Most soils formed in the Mediterranean basin display a distinguishable red color (terra rossa)
88 that derives from high concentrations of ultra-fine pedogenic iron oxides, mainly hematite (Yaalon,
89 1997; Durn et al., 1999). Terra rossa soils receive significant aeolian dust additions from Sahara and
90 Sahel regions (Yaalon, 1997; Durn, 2003; Stuut et al., 2009). In the Mediterranean alpine hinterland,
91 thin drapes of Sahara-dust-rich soils are found on plateaus, glacial moraines, and outwash plains
92 (e.g., Rellini et al., 2009), whereas aeolian dust accretion in terra rossa soils can also originate from a
93 wide range of alluvial deposits, such as sand dunes, desiccated alluvial planes, and Quaternary loess
94 (Amit et al., 2020; Lehmkuhl et al., 2020). Most of the Mediterranean mountains are built up by
95 carbonate rocks, hence the aeolian input to alpine soil formation occurs in parallel with colluvial
96 deposition of carbonate erosion and dissolution products that form a characteristic insoluble residue
97 incorporated in the soil sequences (Durn 2003; Varga et al., 2016; Kirsten and Heinrich, 2022).

98 In the present study, we investigate the major processes that drive the postglacial formation of
99 Mediterranean alpine soils in the periglacial landscapes of Mount Olympus, Greece. We follow a
100 combined sedimentological, mineralogical, and isotopic approach, and present a detailed
101 characterization of distinct alpine sediment and soil horizons developed across a geomorphological
102 gradient of decreasing erosive power. Discrete sediment samples from intact sandy layers
103 interbedded in postglacial stratified scree slope deposits that represent *in situ* erosional products of
104 the periglacial zone of Mount Olympus, are compared with samples from a soil profile developed in a
105 glaciokarstic plateau, with a goal to assess the relative contributions of aeolian dust accretion to the
106 fine fraction of an alpine soil. We differentiate between the physical and chemical processes that
107 drive the production of the scree slope sandy layers and of the alpine soil profile, by comparing their
108 respective grain size distributions, and bulk mineralogy. Furthermore, we examine the potential
109 influence of Sahara and locally sourced aeolian dust accretion on the alpine soil profile by comparing

110 the sedimentological, mineralogical, and radiogenic isotope compositions through the application of
111 $^{86}\text{Sr}/^{87}\text{Sr}$ and $^{143}\text{Nd}/^{144}\text{Nd}$ ratios between the soil samples and Sahara dust samples collected from the
112 snowpack. We finally measured the magnetic properties of the soil samples and clay mineralogy of
113 bottom and topsoil layers, to assess the potential for weathering of clay minerals and iron oxides
114 within Mount Olympus periglacial zone. Understanding the sources of parent materials and soil
115 formation processes between contrasting geomorphological settings is a fundamental step towards
116 defining the postglacial paleo-environmental history of Mount Olympus alpine landscapes that
117 followed pronounced shifts of the regional climate.

118

119 **2 BACKGROUND**

120 **2.1 Mount Olympus glacial history**

121 Mount Olympus is the highest mountain in Greece, rising 2918 m above the northwest coastline of
122 the Aegean Sea (Figure 1a). It is a precipitous massif with a circular shape composed of Triassic to
123 Cretaceous metacarbonates, uplifted along a frontal fault that runs parallel to the present-day
124 shoreline. Mount Olympus is exhumed from the silicate crystalline bedrock, which dominates the
125 lithology of Pieria Mountains (granites, ophiolites) to the north and east, and Mount Olympus
126 granites to the west (Figure 1B). High uplift rates along with successive Quaternary glaciations have
127 created the present-day rugged terrain. The deglaciation of Mount Olympus since the Last Glacial
128 Maximum (LGM), between 28 and 24 ka BP (Allard et al., 2020), triggered the rapid retreat of an ice
129 cap that was covering the summit area and extended down to elevations of ~ 1800 m (Kuhlemann et
130 al., 2008). The post-LGM glacier retreat was intercepted by a glacier re-advance phase at ~ 15 ka BP
131 that was limited at the highest cirques above 2200 m at ~ 12.5 ka BP (Styllas et al., 2018). This latter
132 phase of glacial expanse is traced in both Megala Kazania (MK) and Throne of Zeus (TZ) cirques
133 (Figure 1C). The absence of absolutely dated glacial features between early- and mid-Holocene (9–4
134 ka BP) in both cirques suggests reduced glacial activity, whereas Late Holocene (4 ka BP to present)
135 glacier advances have been observed only in the MK cirque (Figure 1C). These include a terminal

136 moraine stabilization phase at ~ 2.5 ka BP followed by a smaller expansion of the MK glacier at the
137 beginning of the Little Ice Age (LIA) at ~ 0.6 ka BP (Styllas, 2020). Late Holocene glacier advances in
138 the MK cirque lack similarly dated glacial landforms in the TZ cirque, but we cannot rule out the
139 possibility that the Late Holocene climatic shifts towards glacial conditions triggered an
140 intensification of glacial and periglacial processes, which in turn affected the late Holocene landscape
141 evolution, scree slope aggradation and alpine soil production.

142

143 **2.2 Climate**

144 The contemporary maritime conditions and the steep relief of Mount Olympus result in intense
145 precipitation and temperature altitudinal gradients, with the highest peaks constituting an
146 orographic and climatic barrier between the eastern (marine) and western (continental) sides (Figure
147 1b, Styllas and Kaskaoutis, 2018). The climate in the coastal zone is typically Mediterranean, whereas
148 at higher elevations (1000–2200 m), the climate attains sub-Mediterranean characteristics with
149 average annual precipitation of 1300 mm (Styllas et al., 2016). In the alpine zone above the tree line
150 (2400 m), the climate is characterized by temperate conditions with annual precipitation above 2000
151 mm and average annual temperatures between 0 and 1.5 °C (Styllas et al., 2016). The periglacial
152 activity in the Mount Olympus alpine zone is likely still active today, as it is situated just above the
153 lower limit of the regional permafrost zone (2700m) of the southern Balkan peninsular (Dobiński,
154 2005).

155

156 **2.3 The Plateau of Muses**

157 The Plateau of Muses (PM) is a planar depositional surface located at an elevation of 2600 m with a
158 surface area of 1 km². It resembles a typical alpine meadow, partly covered by alpine grass
159 vegetation that shares similar characteristics with plateaus found in the high Balkan Mountains and

160 the European Alps. The PM is bounded to the south by the TZ cirque lateral moraine ridge and by
161 several gentle-sloping glacially eroded peaks along its northern, eastern, and western margins (Figure
162 1C). The formation of the plateau has resulted from the combined action of glacial scouring and
163 carbonate bedrock dissolution. Its low relief in combination with the circular shape suggest a doline
164 type karstic depression that is filled with glacial till, overlain by colluvial sediments (slope wash)
165 transported from the adjacent slopes. The surface layer of the PM sedimentary sequence comprises
166 a developed soil sequence with variable thickness (30–50 cm) that overlies a layer of outwash sand
167 and fine gravels and/or fragmented till boulders, and exhibits brown-red to yellow color hues, which
168 in the Munsell color scale range between 7.5 and 10 YR (Table 1). Alternating patches of alpine grass
169 vegetation and hummocky soil pans in the center of the plateau are indicative of periglacial activity
170 and cryoturbation. Other periglacial features such as solifluction-terraced stripes below the bare
171 bedrock of the surrounding summits are tentatively considered to have formed during the Late
172 Holocene cold stages, during the observed expansion of small glaciers in the MK cirque.

173

174 **3 MATERIALS AND METHODS**

175 **3.1 Erosional products and alpine soil sampling**

176 To adequately address the question of the relative balance between aeolian dust accretion and local
177 erosion of moraines and scree slopes to the development of the alpine soil on Mount Olympus
178 periglacial zone, a wide range of methods were employed and involved the analyses of 21 discrete
179 soil and sediment samples retrieved along a transect of decreasing hillslope energy and erosional
180 power (Figure 2). Five samples (n=5) were retrieved from clast-free sandy horizons interbedded in
181 the relatively young (Late Holocene) MK and older (early Holocene) TZ stratified scree slopes, and
182 sixteen (n=16) were sampled from the PM soil sequence at 2-cm intervals (Table 1). The specific
183 experimental setting was selected to evaluate the impact of physical weathering on providing the
184 base material for the development of the PM soil. We only sampled naturally exposed clast free
185 sandy layers found within the scree slopes of MK and TZ. We considered that these layers share

186 similar textural, mineralogical, and geochemical characteristics with the PM soil basal horizon, which
187 lies on a layer of outwash sand and gravels. Luckily, we were able to retrieve the samples from two
188 distinct interbedded clast free sediment layers within the TZ scree slope after a torrential rainfall
189 event that opened a deep erosional trench in the scree below the rockwall and reached the basal till
190 layer (Figure 2). The scree slope in the MK is regularly eroded and scoured from a perennial snowfield
191 that is retreating by the end of the summer season, and this made the sampling of distinct soil-
192 sediment horizons straightforward. We manually excavated only one pit for high resolution soil
193 sampling and considered that due to the very small surface area of the surficial soil apron within the
194 PM catchment (0.06 km²), the specific profile is representative of the PM soil development. We
195 selected a location in the center of a circular soil-sediment pan that was free of vegetation, surface
196 carbonate fragments (Figure 2). After sampling, the pit was closed and refilled with the excavated
197 material in accordance with Mount Olympus National Park directions. In locations with long lasting
198 snowpack, we observed a humic A horizon, but since these locations host several endemic flower
199 species, the Management Unit of Mount Olympus National Park, did not grant permission to
200 excavate a soil pit in these sensitive sites. The PM soil samples were additionally subjected to
201 microscopic and radiogenic isotope analyses and magnetic measurements to investigate the
202 potential chemical alterations processes during PM soil development. Mineralogical and radiogenic
203 isotope analyses were also performed in two (n = 2) samples of aeolian dust that were deposited on
204 the PM snowpack during the spring seasons of 2018 and 2022. The long-range aeolian dust transport
205 episodes occurred on March 22–24, 2018, and March 16–18, 2022. The synoptic conditions of these
206 distinct episodes show that the dust emissions traveled to Mount Olympus from the Sahara Desert
207 and left an orange hue on the snowpack, which later in the spring season formed distinct layers in
208 the snowpack (Figure 3). We therefore consider the samples collected from the PM snowpack as
209 representative of Sahara dust accretion in Mount Olympus alpine soils.

210

211 **3.2 Grain size analyses**

212 The soil samples were transported to the lab, wet sieved through a 3.5-mm sieve, and treated with
213 30% hydrogen peroxide (H₂O₂) at 70 °C for 12 h to remove organic matter. The H₂O₂ treatment was
214 repeated three times until the samples were completely bleached and all organic matter was
215 degraded. The samples were washed with distilled water and analyzed with a Mastersizer 3000 laser
216 diffraction particle-size analyzer to define the bulk grain size distributions of the sand, silt, and clay
217 fractions. The samples were run through the automated dispersion unit and sodium
218 hexametaphosphate solution (Calgon) was added as dispersion factor. Statistical analyses of the grain
219 size distributions and derivation of the clay, silt, and sand fractions were realized with MATLAB Curve
220 Fitting Lab (CFLab), which performs curve fitting on sediment grain size distributions using the
221 Weibull probability distribution function (Wu et al., 2020).

222

223 **3.3 Mineralogy**

224 Identification of the mineral phases of the soil and aeolian dust bulk samples was achieved through
225 X-ray diffraction (XRD, Philips diffractometer PW1800, Co radiation at 40 kV and 40 mA), and two
226 samples from the top and base of the PM soil profile (PM1 and PM15) were additionally analyzed for
227 their clay (<2 μm) mineralogy through ethylene glycolation and heating for 2 h at 550 °C. The PM soil
228 samples semi-quantitative composition of the main mineral phases (e.g., quartz, feldspar,
229 plagioclase, micas, calcite) was determined using MAUD-Material Analysis software applied for full
230 pattern Rietveld refinement (Lutterotti et al. 2007) and is expressed as weight percent (wt %)
231 concentrations.

232

233 **3.4 Petrographic, magnetic, and isotopic analyses**

234 Additional analytical methods were applied only to the PM soil samples to assess the potential sources
235 of soil-forming material, pedogenesis, and chemical weathering. The fabric configuration of the PM
236 alpine soil was explored through scanning electron microscopy–energy dispersive spectrometry
237 (SEM–EDS) analyses (JEOL JSM-840A equipped with an INCA 250; Oxford) with a 20-kV accelerating

238 voltage and 0.4-mA probe current. Backscattered electron images (BSE) enabled us to detect the
239 shapes of different minerals, and the physical weathering features of specific grains, whereas with
240 the EDS analysis we examined areas of different chemical composition within the same soil
241 aggregates.

242 We additionally explored the existence of ferromagnetic components and the potential for
243 secondary iron oxides formation in the PM soil profile through magnetic susceptibility
244 measurements. The discrete samples were packed in cubical plastic boxes ($2 \times 2 \times 2$ cm) and weighed
245 before the measurements. Volume-specific magnetic susceptibility measurements were performed
246 using both a Bartington dual MS2B sensor at low and high frequencies of 0.465 and 4.65 kHz. The
247 results are expressed as mass-specific magnetic susceptibility (χ ; 10^{-8} m³/kg). During the measuring
248 procedure, every sample was measured at least three times and the average value was assigned as
249 the final measurement. For each sample, two air measurements were performed before and after
250 sample measurement. The frequency-dependent susceptibility (χ_{FD} ; %) was calculated according to
251 Dearing et al. (1996):

$$\chi^{FD}\% = \frac{100(\chi_{LF} - \chi_{HF})}{\chi_{LF}} \quad (1)$$

252
253 where χ_{LF} , χ_{HF} , are the magnetic susceptibility at low and high frequency, respectively. Samples PM16
254 and PM15, which were considered as more representative of the PM soil regolith boundary, were
255 additionally subjected to thermomagnetic analysis to define the origin of the ferromagnetic particles
256 at the base of the PM soil. Measurements of continuous thermomagnetic curves (K–T curves) at low
257 and high temperature were realized with the furnace CS3 of the AGICO MFK1-FA susceptibilimeter.

258 The potential sources of the PM soil and aeolian dust were evaluated through their Sr and Nd
259 isotopic ratios. Isotopic measurements were performed at the University of Arizona TIMS laboratory
260 following the procedure in Conroy et al. (2013) on soil samples. Samples were not spiked and
261 dissolved in mixtures of ultrapure Hf-HNO₃ acid. Elemental separation of dissolved samples was
262 carried out in chromatographic columns via HCl elution in a clean laboratory environment.
263 Conventional cation columns filled with AG50W-X4 resin were used for Sr and REEs separation and

264 anion columns with LN Spec resin for Nd separation following Ducea et al. (2020). Sr cuts were
265 loaded onto Ta single filaments and Nd cuts onto Re filaments. $^{87}\text{Sr}/^{86}\text{Sr}$ and $^{143}\text{Nd}/^{144}\text{Nd}$ ratios (Table
266 3) were measured on a VG Sector 54 thermal ionization mass spectrometer (TIMS) fitted with
267 adjustable 1011 Ω Faraday collectors and Daly photomultipliers. NBS SRM 987 Sr standard and La
268 Jolla Nd standard were analyzed during the samples run to ensure the performance of the
269 instrument and to perform some minor correction on the final reported ratios.

270

271 **3.5 Erosional potential and aeolian dust accretion proxies**

272 The erosional potential of the three sampling sites, which are distanced along a 2km transect was
273 derived from field estimates of the vertical height of the MK and TZ rocky headwalls and their scree
274 slopes. We evaluated the plateau and scree slope energy distribution and maturity stage from the
275 dimensionless ratio between the vertical height of the scree slope (H_t) to the vertical height of the
276 headwall (H_c) following Statham (1976) (Figure 2).

277 To assess the potential contribution of distal and local aeolian dust inputs in the PM soil we used
278 the contents of quartz (wt. %). The source of quartz can be local, from the Pieria Mountains silicate
279 bedrock and from the granites to the west of Mount Olympus, or can be transported during Sahara
280 dust episodes, as evidenced from the XRD analyses of the PM snowpack samples, which are in line
281 with Sahara dust samples from the Pyrenees, the European Alps, and the Carpathian Mountains that
282 contain high amounts of quartz (e.g., Rellini et al., 2009; Rodriguez-Navarro, 2018; Marmureanu et
283 al., 2019). Herein, we cannot exclude the possibility of quartz release from the local bedrock through
284 periglacial erosion, but the amount of quartz released from local bedrock dissolution is expected to
285 be small, wt.% concentration of the insoluble residue from carbonates in Greece is less than 1%
286 (MacLeod, 1980; Kantiranis, 2001; Kirsten and Heinrich, 2022). Therefore, it is reasonable to consider
287 quartz (wt. %) as a reliable proxy of aeolian dust accretion.

288 We selected the ϵ_{Nd} ratio as a second independent proxy particularly of Sahara dust accretion
289 in the PM soil. We did not use the Sr ratio ($^{87}\text{Sr}/^{86}\text{Sr}$) as it can be impacted by the dissolution of

290 carbonate particles and replacement of Ca by Sr during pedogenetic alteration of the PM soil (e.g.,
291 Shalev et al., 2013). Sr isotopic distributions of PM soil can be further complicated by the accretion of
292 sea-salt Sr through orographic precipitation (Kurtz et al., 2001). Rain is not a significant source of Nd,
293 so the addition of rainwater and snow should not affect the Nd isotopic composition of the aeolian
294 dust, so ϵ_{Nd} is buffered against these changes (Kurtz et al., 2001). We estimated the fraction of
295 Sahara dust from the ϵ_{Nd} ratios of the PM soil, the dust deposited on the snowpack, and the local
296 bedrock following the method by Kurtz et al (2001):

297

$$298 \quad f = \frac{(\epsilon_{Nd} \text{ PM soil} - \epsilon_{Nd} \text{ bedrock})}{(\epsilon_{Nd} \text{ Sahara dust} - \epsilon_{Nd} \text{ bedrock})} \quad (2)$$

299 As we had not obtained direct Sr and ϵ_{Nd} values from Mount Olympus bedrock, we used the value of
300 the basal sample PM 16, which is dominated by bedrock derived calcite and falls in the same value
301 range with basin-average values of terrestrial, coastal, and marine sediments deposited in the
302 Aegean Sea (Weldeab et al., 2001).

303

304 **4 RESULTS**

305 **4.1 Alpine soil formation across a hillslope energy gradient**

306 According to Statham (1976), Ht/Hc values above 0.4 characterize a mature scree slope, which is the
307 case for the TZ (0.6) but not for the MK (0.3) scree slope, and this reflects the older deglaciation age
308 of the TZ cirque (~12.5 ka BP, Section 2.1). The MK scree slope is deposited behind the LIA moraine
309 (Figure 1C), so that the most recent deglaciation processes (~0.6 ka BP to present) has resulted in
310 immature scree development. Conversely, the low-relief, low-erosion PM acts as a long-term
311 depocenter of slope wash and detrital (aeolian and bedrock derived through freeze-thaw action)
312 sediments. For this low-energy setting, we believe that minor colluvial contributions, cryoturbation,
313 aeolian dust accretion, fine earth translocation, and post-depositional mineral alteration are the
314 major drivers of PM soil production. The irregular boundary between the base of the PM soil and the

315 underlying regolith composed of glacial till and outwash gravels, is indicative of cryoturbation, while
316 observations of late-season soil freezing and waterlogging (Figure 4) provide permissive evidence
317 that PM soil development is disturbed by cryogenic processes. The energy gradient along the
318 contrasting environments impacts the soil color. The PM soil basal layer overlying the regolith shares
319 similar color characteristics with the MK samples and with the TZ upper sediment horizon, which
320 have grey to olive green hues (Munsell dry color 2.5– 5 Y; Table 1). Conversely, the lower clast-free
321 sediment horizon of the TZ scree shares similar Munsell dry color characteristics with the PM soil,
322 characterized by red-brown to yellow hues (7.5–10 YR, Table 1), suggesting that these soil samples
323 are more oxidized and are undergoing pedogenetic alterations.

324

325 **4.2 Grain size variation**

326 The interactions between slope processes, colluvial sediment transport, and aeolian sub additions
327 result in polymodal grain size distributions that display different shapes among MK, TZ, and PM soils.
328 Five grain size modes (M1 to M5) were mathematically derived from the application of the CFLab
329 curve-fitting algorithm. Fitting degrees were >99% and fitting residuals were <0.1%, indicating
330 excellent fits for the raw grain size distribution curves (Figure 5 A, B, C, and D). The fine-earth (clay
331 and silt) fractions resemble grain size modes M1 and M2 with respective mean grain sizes of ~ 2 and
332 ~ 4 μm and M3 with mean grain sizes between 10 and 30 μm . The sand fraction is composed of two
333 modal sub-populations: a fine-sand-grain size mode (M4, mean grain size ~ 80 μm) and a coarse
334 sand-grain size mode (M5, mean grain size 440 μm) (Figure 5 E, F, G, and H; Table 1). The production
335 of coarse sand is transported to the respective interbedded sediment horizons by rockfall activity and
336 colluvial processes, or in the case of the low-sloping PM, through slope wash. The fine sand (M4)
337 subpopulation was not traced in the PM soil samples, and this can be linked to either selective
338 entrainment of M4 or to distortion of the MK and TZ grain size curves and truncation of the coarser
339 modes (Garzanti et al., 2009).

340 In addition to the distinct color variations, the contrasting slope-energy distribution between the
341 MK, TZ scree slopes and the PM depositional environments also defines their textural compositions.
342 Sediment horizons developed on the surface of the MK scree slope contain higher amounts of sand
343 (~90%) and lower amounts of silt and clay (~10%) compared with their TZ counterparts (~75% and
344 ~25%), implying that the dominance of sand in the sediment horizons of the scree slopes derives
345 from freeze-thaw and colluvial activity. The coarse-sand content (M5) of the PM soil basal layer is 6%
346 but is lower within the solum (2%–3%), suggesting either reduced periglacial activity and/or low
347 transport capacity of erosional products from the catchment through slope wash processes during
348 the PM soil formation (Table 1; Figure 2, lower graphs).

349 The grain size distribution curves of the PM soil present a significant change in shape between
350 soil depths of 14 and 16 cm, which is characterized by a 15% reduction of the clay and very-fine-silt
351 fractions (M1 and M2) and by a similar increase of silt contents (Figure 5A and B). This sharp textural
352 differentiation was not supported from field observations, where the solum appeared homogenous
353 without distinct pedogenetic horizons and without any visual evidence of an erosional layer (Figure
354 6A), but it is supported by changes in the soil color. The samples above a soil depth of 14–16 cm
355 exhibit red to brown hues (7.5 YR), whereas the samples below this layer have more yellow-red (10
356 YR) hues (Table 1). We also observed clay coatings in sparse secondary carbonates (calcretes) along
357 the lower part of the PM soil profile, which we interpret as evidence of soil mixing and downward
358 translocation of dissolved Ca and secondary calcite precipitation at the base of the soil profile. Based
359 on these observations, we partitioned the PM soil profile in two horizons: an upper Bw horizon
360 between 0 and 14 cm with red to brown hues, low clay (~25%), and high silt (~75%) contents, and a
361 lower illuvial Bt horizon between 14 and 32 cm with higher (~40%) clay contents, a yellow-red hue,
362 and smaller amounts (~5%) of sand compared with the overlying Bw horizon (Figure 6).

363

364

365 4.3 Soil and aeolian dust mineralogy

366 XRD analysis of the bulk samples reveals a mineralogy that substantially differs between the MK,
367 TZ, and PM soils and, like the soil colorization and textural variations, follows the erosional slope
368 gradient. The most dominant mineral phase in the clast-free material of the MK and TZ soils is calcite.
369 Other minerals identified include dolomite along with quartz and micas. Conversely, the bulk
370 mineralogical composition of PM soil exhibits a richer matrix of minerals that includes quartz, chlorite
371 and mixed layer clays, mica, potassium feldspars, and plagioclase (Figure 7). Calcite is dominant
372 (~50%) only in basal sample PM16 (Figure 6; Table 2). Quartz, clays, and mica are the most dominant
373 mineral phases in the PM soil (~80%) with low values in basal sample PM16, whereas plagioclase, K-
374 feldspar, and mica represent the remaining 20% (Table 2). Semi-quantitative analysis of the clay
375 mineralogy of two samples retrieved from the surface of the Bw horizon and the base of the Bt
376 horizon (samples PM1 and PM15) revealed high concentrations of smectite and kaolinite (80%) and
377 low contents of chlorite and illite. Surface sample PM1 contains 45% smectite and 35% kaolinite,
378 whereas basal sample PM15 has higher smectite (65%) and lower kaolinite (25%) contents (Table 2).

379 From the comparison of the XRD spectra (Figure 7), it is obvious that the bulk mineralogy of the
380 PM soil matches that of the Sahara dust samples. Both Sahara dust samples show the presence of
381 clay minerals, quartz, mica, calcite, plagioclase, K-feldspar, and dolomite. The detected mineral
382 phases are typical of Saharan dust deposited in Europe during both dry- and wet-deposition (red
383 rains) events (Scheuvens et al., 2013). Additionally, recent studies of Saharan dust wet deposition in
384 the Iberian Peninsula also indicated the presence of Fe-Ti oxides, such as goethite and hematite, and
385 of Ti oxides, such as rutile (Rodriguez-Navarro et al., 2018), but these were not depicted from our
386 XRD analyses. Despite their overall XRD spectral similarity, a pronounced difference between the
387 contemporary Sahara dust and PM soil samples is the presence of calcite and dolomite in the dust
388 samples and their near absence from the PM soil profile (Figure 7). The smooth and low intensity
389 peaks for calcite and dolomite at 29.43 and 30.7 2 θ in surface sample PM1 indicate the partial

390 removal of calcite, whereas similarly subdued peaks in basal sample PM16 denote near complete
391 decalcification of the solum (Figure 7).

392

393 **4.4 Magnetic susceptibility of PM soil**

394 The magnetic susceptibilities of the PM soil bulk samples were measured to provide insight into the
395 ferromagnetic components of the PM soil and their potential alterations. Overall, the low-frequency
396 magnetic susceptibility (χ_{lf}) is higher in the lower Bt horizon, with average values for samples PM8–
397 PM16 of $55 \times 10^{-8} \text{ m}^3 \text{ kg}^{-1}$, and lower χ_{lf} values in the Bw horizon, with average values for samples
398 PM1–PM7 of $36 \times 10^{-8} \text{ m}^3 \text{ kg}^{-1}$ (Figure 8A). Similar value ranges were measured for the high-
399 frequency magnetic susceptibility (χ_{hf}). The estimated values of frequency-dependent (χ_{FD})
400 susceptibility presenting a wide range of values ranging between 0% (sample PM13) and 14%, with
401 significantly higher values in the Bw horizon (Figure 8B). According to Dearing (1999), high χ_{FD} values
402 (>10%) are indicative of the presence of superparamagnetic Fe oxide nanoparticles (< 0.05 μm),
403 suggesting a higher amount of fine ferrimagnetic grains in the surface horizon Bw, which potentially
404 can be of detrital (aeolian and/ eroded bedrock) origin.

405 The mineral phases responsible for the magnetic enhancement of the Bt horizon were deduced
406 from high-temperature magnetic susceptibility measurements performed during a single heating–
407 cooling cycle to 700 °C (Figure 8C). We estimated the Curie temperature (T_c) of samples PM16 and
408 PM15 to examine the potential existence of superparamagnetic ultrafine particles in the base of the
409 PM soil profile, which is in contact with the regolith. The thermomagnetic analysis of sample PM16
410 failed completely, likely due to its high calcite content and absence of magnetic phases. On the other
411 hand, sample PM15 resembling the soil-regolith lower boundary, revealed a uniform χ -T behavior
412 that is indicative of the dominance of two magnetic phases (Figure 8C) – one with T_c , or
413 transformation temperature, between 260–320 °C, probably maghemite, and a second one around
414 600 °C, which is typical for oxidized magnetite (Jordanova et al., 2022). Since the nano-sized

415 pedogenic magnetite is unstable upon heating (Dunlop and Özdemir, 1997), the identified oxidized
416 magnetite suggests that weak pedogenetic production of ferromagnetic components occurs in the
417 base of PM soil profile.

418

419

420 **4.5 Radiogenic isotopes**

421 More information on the provenance of the PM-soil-forming material was derived from the
422 radiogenic isotope analysis of the soil samples and of the 2018 Sahara dust sample. The $^{87}\text{Sr}/^{86}\text{Sr}$
423 values of PM soil samples range from 0.71437 to 0.72071 and the ϵ_{Nd} values from -7.75 to -9.80
424 (Table 3). Overall, the PM soil $^{87}\text{Sr}/^{86}\text{Sr} - \epsilon_{\text{Nd}}$ cluster together apart from sample PM16, which has the
425 lowest value of the PM soil $^{87}\text{Sr}/^{86}\text{Sr}$ ratio (Figure 9). The analyzed Sahara dust sample exhibits
426 $^{87}\text{Sr}/^{86}\text{Sr}$ value of 0.71272 that falls within the lower range of North African dust sources between
427 ~ 0.71200 and 0.74000 (Erel and Torrent, 2010; Grousset and Biscaye, 2005). The Sr isotopic ratio of
428 the Sahara dust sample shows potential mixing with rainwater and local sea salt aerosols during the
429 March 2018 wet deposition event but also with other European aerosol sources, which is validated
430 by the fact that the dust plume of the March 2018 travelled over Europe before it reached Mount
431 Olympus (Figure 3A). The Sahara dust sample has an ϵ_{Nd} value of -6.80 . Plotting the $^{87}\text{Sr}/^{86}\text{Sr}$ and ϵ_{Nd}
432 measurements against literature values from terrigenous, coastal, and marine sediments from the
433 Aegean Sea region (Weldeab et al., 2002) reveals an isotopic similarity between the Sahara dust and
434 of sample PM16 with these sediments (Figure 9). A reasonable interpretation of this observation
435 comes from the fact that basal sample PM16 resembles more the soil regolith and plots close to the
436 contemporary and Holocene values of Aegean Sea terrestrial, coastal and marine sediments. The
437 $^{87}\text{Sr}/^{86}\text{Sr}$ values representing the PM soil regolith show similar values with the Aegean Sea terrestrial
438 and marine sediments and likely represent a mix of Sahara dust with Mesozoic and Cenozoic bedrock
439 carbonates, which are overall characterized by low $^{87}\text{Sr}/^{86}\text{Sr}$ values of <0.70800 (Capo et al., 1998;
440 Frank et al., 2021). The two subclusters of PM soil samples have more radiogenic values compared

441 with those of the rest of the samples and clearly correspond to Bw and Bt horizons. The increasing
442 silt contents towards the surface of the PM soil profile (Figure 6, Table 1) occur with $^{87}\text{Sr}/^{86}\text{Sr}$ and ϵ_{Nd}
443 values towards more crustal values (color variation in Figure 9) that are representative of the central
444 Sahara province. Therefore, the increases in the silt fraction within the PM soil profile can be directly
445 linked to increases in Sahara dust accretion. This is further supported by range of the silt fraction
446 mean grain size between 14 and 30 μm (Table 1), which is similar to those for modern Sahara dust
447 deposits from Crete, which range 4–8 μm and 16–30 μm (Mattson and Niéhlen, 1996; Goudie and
448 Middleton, 2001). In terms of Sahara dust provenance fingerprinting, the $^{87}\text{Sr}/^{86}\text{Sr}$ and ϵ_{Nd} values of
449 the PM soil samples fall within the range (1σ) of the central North African dust source area, which
450 broadly involves the Bodele depression (PSA2; Jewell et al., 2021).

451

452 **5 DISCUSSION**

453 **5.1 PM soil parent material**

454 The mineralogical (XRD) analyses, show that calcite is the dominant mineral phase of MK and TZ
455 interbedded sandy sediment and PM basal layers (Figure 7, lower XRD diagrams TZ01 and Table 2
456 sample PM 16), which in the periglacial environment of Mount Olympus is expected to dissolve
457 slowly (e.g., Gaillardet et al., 2019) and produce an insoluble residue that comprises the PM soil
458 parent material. MacLeod (1980) analyzed the mineral composition of the insoluble residue of
459 carbonates from western Greece and defined a mineralogical suite of quartz, kaolinite, and mica
460 (illite). Kantiranis (2001) studied the carbonate rocks of northwestern Greece and found insoluble
461 residue ~1wt.% consisting mainly of micas, quartz, hematite, chlorite, feldspars, and amphibole,
462 whereas the insoluble residue of carbonate basement rocks from Crete also resembles ~1 wt.% of
463 the whole rock samples and is composed of a sandy loam matrix rich in quartz, plagioclase (albite),
464 and mica (illite) (Kirsten and Heinrich, 2022). Thus, the dissolution of the local carbonate parent
465 material within the interbedded sediment layers and in the basal layer of PM soil, can release very

466 small quantities of bedrock-derived impurities such as quartz, plagioclase, illite, and kaolinite that are
467 incorporated in the solum, but cannot explain the ~30cm thick PM soil mantle and ~60cm thickness
468 of the layers interbedded in the scree slopes.

469 It has also been proposed that clay in terra rossa soils can derive from isovolumetric
470 replacement of calcite to authigenic clays across a metasomatic front, but this mechanism requires
471 significant input of aeolian dust to provide essential elements such as Al, Si, Fe and K for clay
472 formation (Merino and Banerjee, 2008). Even though we did not estimate the dissolution rate of
473 Mount Olympus bedrock metacarbonates and the elemental composition of the insoluble residue,
474 we consider that the fine earth (silt and clay) contents of MK and TZ interbedded layers, which
475 average 10% and 25%, respectively, cannot be derived only by carbonate dissolution and/or by
476 isovolumetric replacement of calcite. Küfmann (2008), Krklec et al. (2022) and Ott et al. (2023)
477 propose carbonate bedrock dissolution rates between ~0.23, 0.15 and 0.4 cm/ka respectively, which
478 for the postglacial (12.5 ka BP to present) alpine soil formation on Mount Olympus imply ~5 cm of
479 carbonate loss to soil formation, a value too low to explain the observed thickness of MK, TZ,
480 interbedded layers and PM soil as a result of residual clay accumulation alone. Our direct
481 observations of episodic Sahara dust deposition on the snowpack of Mount Olympus (Figure 3)
482 provide undisputable evidence of Sahara dust accretion on PM soil. The relative contribution of local
483 dust from moraines, outwash plains and from silicate bedrock formations in the vicinity of Mount
484 Olympus is estimated in the following section, but irrespective of the relative dust sources (Saharan
485 and local), the high-energy erosive regime of Mount Olympus alpine critical zone intercepts the
486 formation of extensive aeolian dust mantles, like the one found on the stable Plateau of Muses. We
487 thus suggest that the production of silt, and clay in the PM soil basal layer, partly reflects the
488 contribution of mechanically produced sandy and fine earth carbonate debris and its dissolution
489 products, which together with aeolian dust accretion, comprise the parent materials for the PM soil
490 production.

491

492 **5.2 Relative contributions of aeolian dust inputs**

493 Studies on terra rossa soils in Greece, with typical bimodal grain size distributions consisting of clay
494 and silt subpopulations with grain size ranges of 2–4 and 10–40 μm , respectively, ascribe the clay
495 fraction, which is rich in illite and kaolinite, to the limestone residue, and the silt fraction, which is
496 made up entirely of quartz, to long-range aeolian transport from variable sources (Russel and Van
497 Andel, 2003). In line with this notion, we considered the quartz wt. % content in the solum, as a
498 proxy for aeolian dust in general and not exclusively of Sahara dust. The rounded shape of quartz
499 grains observed in SEM images (Figure 11D), provides supplementary evidence for the aeolian
500 transport of quartz grains. Furthermore, we consider that the neodymium-derived mass fraction (f),
501 solely a proxy of Sahara dust accretion in the PM soil. This is supported by the high statistical
502 correlation between the silt fraction (M3) with the ϵ_{Nd} -derived f fraction ($R^2= 0.73$, $P < 0.001$) and by
503 the similarity of the grain size ranges between the silt fraction and the modern Sahara dust deposits.
504 The mass fraction (f) of Sahara-dust-derived ϵ_{Nd} was calculated based on the highest ϵ_{Nd} value of
505 sample PM 16 and Aegean Sea sediments ($\epsilon_{\text{Nd}} = -5.94$) and on the lowest value of Sahara dust PSA2
506 ($\epsilon_{\text{Nd}} = -13.81$) end members. The ϵ_{Nd} value of Aegean Sea sediments is considered conservative in
507 relation to that of Mount Olympus bedrock due to the mixing of the carbonate bedrock sediments
508 with other sources of silicate bedrock during fluvial transport.

509 The ϵ_{Nd} -based Sahara dust contributions to the PM soil varies between $\sim 35\%$ and $\sim 50\%$
510 (except that of basal sample PM16) (Figure 10). Conversely, the quartz-derived aeolian dust
511 contribution ranges between $\sim 45\%$ and 65% , shows a relatively small variation with depth and an
512 abrupt increase ($\sim 25\%$) from sample PM16 to PM15 (Figure 10). The basal sample PM16 exhibits the
513 lowest contributions of quartz concentration, f ratio values (Figure 10) and silt concentrations (Table
514 1, Figure 6) and is considered an outlier representing the regolith-PM soil mix, which agrees with its
515 distinct color and lowest magnetic susceptibility values. The preservation of quartz in the PM soil

516 profile and especially in the lower Bt horizon requires a mechanism of reduced Sahara dust input
517 and/or loss to weathering, with simultaneous inputs of other quartz-rich-derived dust. A pattern that
518 can explain the lower ϵ_{Nd} -based Sahara dust contributions in the Bt horizon and the near steady
519 quartz contents is a shift in atmospheric circulation patterns that resulted in less-frequent dust
520 transport episodes from north Africa along with steady aeolian quartz accretion from local quartz
521 sources. Aeolian quartz from the silicate bedrock formations of the Pieria mountains, Mount
522 Olympus granites and even from the Katerini alluvial plane (Figure 1) can be deposited on Mount
523 Olympus periglacial zone during periods of regional aridity, associated with thinning of vegetation,
524 desiccation of the Katerini alluvial plane, and immobilization of fine dust grains through convection.

525 Based on the above, we tentatively attribute the $\sim 15\%$ difference between the ϵ_{Nd} -based
526 estimates and the quartz-based estimates to accretion of quartz-rich dust from local sources during
527 the formation of the Bt horizon, considering that the contribution of bedrock derived quartz from
528 the insoluble residue is $\sim 1\%$. From the ϵ_{Nd} -based contributions, we estimate that the Sahara dust
529 accretion to PM soil is between $\sim 35\%$ to 50% , whereas local sources can potentially accrete another
530 $\sim 15\%$. Our estimated aeolian dust accretion $\sim 65\%$ is similar to the one in the North Calcareous Alps,
531 where the local contribution of dust from the periglacial zone of the North Calcareous and Austrian
532 silicate Alps is significant (Küfmann 2008), but our estimated Sahara dust contribution in the PM soil
533 is higher than its respective average contribution ($20 - 30\%$, Varga et al., 2016) in interglacial soils of
534 the Carpathian Basin. We attribute this difference to the closer proximity of Mount Olympus to
535 Sahara Desert than the Carpathian basin. Given that these values are conservative estimates, the
536 aeolian contribution may potentially be higher as, in our calculations, we have not included aeolian
537 transported micas, feldspars, and clays that are integral parts of Sahara dust samples deposited on
538 the snowpack. We thus suggest that the aeolian dust accretion comprises a minimum of $\sim 65\%$ of the
539 PM soil parent material and that carbonate bedrock erosion, and pedogenetic production of detrital
540 clays can potentially contribute another $\sim 35\%$ to the development of PM soil.

541

542 **5.3 Pedogenetic alterations**

543 An alternative mechanism that can explain the nearly homogeneous depth distribution of quartz
544 (Figure 10) is soil mixing by cryoturbation and subsequent translocation of fine earth particles from
545 the upper Bw to the lower Bt horizon. The mechanism of illuviation does not necessarily cancel the
546 climatic forcing of Sahara dust reduction and increase of local dust inputs during the development of
547 Bt horizon, but rather can act synergistically. For example, a cold and arid climatic phase that
548 immobilizes quartz-rich dust from the Mount Olympus and Pieria mountains piedmonts can also
549 reactivate the periglacial processes on the Mount Olympus alpine critical zone, which in turn
550 enhance scree slope aggradation, colluvial activity, intensification of freeze–thaw cycles, and
551 cryoturbation of the soils. Cryogenically induced translocation of detrital (aeolian and bedrock
552 derived) silt and clays deposited on the surface of the Bw horizon, distorts the textural composition
553 and soil properties and results in massive structures like the one we observed in the PM soil profile
554 (Figure 4).

555 Despite the absence of color difference and of distinct layers in the PM soil, the higher magnetic
556 susceptibility values of the Bt compared to the Bw horizon, can result from the enrichment of
557 ferromagnetic minerals during *in situ* weathering of translocated detrital fine earth particles through
558 pedogenesis (Maher, 2011). However, the overall low values of the frequency dependent magnetic
559 susceptibility ($\chi_{FD} < 10$), point to weak pedogenetic alteration of soil (Dearing et al., 1996), which in the
560 base of PM soil profile occurs through the oxidation of ultrafine (titano)magnetite to maghemite
561 (Section 4.4). The SEM-EDS analyses show the presence of ultrafine Fe-Ti grains throughout the
562 solum (Figure 11B) apart from basal sample PM16 (Figure 11A), which is representative of the PM
563 soil regolith. This is further supported from the EDS chemical composition of the calcite grains in
564 basal sample PM 16 that have TiO₂ weight % concentration <1%. On the other hand, magnetite is
565 found attached to clay minerals of the Bodéle depression surface sediments (Moskowitz et al., 2016),
566 which is the major source of Sahara dust in PM soil (Figure 10). Also, magnetic susceptibility

567 measurements of Sahara dust modern deposits in SE Bulgaria show a low frequency magnetic
568 susceptibility value of $\chi_{if}=97 \times 10^{-8} \text{ m}^3 \text{ kg}^{-1}$ (Jordanova et al., 2013), which is close to the values of Bw
569 horizon ($\chi_{if}=86 \times 10^{-8} \text{ m}^3 \text{ kg}^{-1}$) and Sahara dust episodes are known to transport Fe-Ti oxides in the
570 Mediterranean region (Rodriguez-Navarro et al., 2018). We can therefore ascribe the observed Fe-Ti
571 oxides and (titano)magnetite an aeolian origin, from either the local igneous silicate outcrops, or the
572 Sahara Desert. Collectively these observations imply that the magnetic enhancement of Bt compared
573 to Bw horizon can result from a combination of fine earth illuviation of aeolian transported ultrafine
574 magnetic particles from the Bw horizon to the Bt horizon through cryoturbation and subsequent
575 weak pedogenetic modifications that result to the oxidation of magnetic minerals like
576 (titano)magnetite and can also explain the reddish to yellow color hues.

577

578 **5.4 Mineral weathering**

579 In addition to the weak pedogenesis of ferromagnetic minerals in the base of the PM soil profile, we
580 assessed the mineral weathering potential of non-magnetic minerals through the clay mineralogy
581 composition of basal and topsoil samples PM15 and PM1. Both samples show the dominance of
582 smectite with lesser contributions by kaolinite, chlorite, and illite (Table 2). High amounts of smectite
583 in alpine soils result from the alteration of detrital chlorite and micas deposited on glacier surfaces
584 and are found in proglacial fields in the European Alps and Rocky Mountains (Egli et al., 2003; Egli et
585 al., 2011; Munroe et al., 2015), so that the 20% difference in smectite concentration (Table 2)
586 between the basal and topsoil layers of PM soil can be partly related to enhanced mineral chemical
587 weathering in the base of the solum. Similarly, kaolinite observed in the XRD profiles of the MK, TZ
588 and Sahara dust samples (Figure 7), can be released from the dissolution of bedrock carbonates, as
589 are the cases for western Greece (Macleod, 1980) and Crete (Kirsten and Heinrich, 2022), but can
590 also form through the alteration of other detrital minerals, such as plagioclase (albite), a process that
591 is common in glacial and periglacial environments (Anderson, 2000). Finally, high smectite and

592 kaolinite contents can also be transported during Saharan dust transport episodes (e.g., Scheuvens et
593 al., 2013), but specifically they are representative of the western Sahara dust provenance (PSA 1, Figure
594 10; Rodriguez-Navarro et al., 2018). However, smectite and kaolinite are also found in modern
595 Sahara dust samples deposited in Athens, Greece (Remoundaki et al., 2011). Therefore, we consider
596 that the high (>80%) concentration of smectite and kaolinite in the PM soil clay (< 2 μm) fraction
597 reflects the balance between direct aeolian deposition and *in-situ* weathering of detrital (aeolian
598 and/or bedrock derived) micas and plagioclase, but the respective contributions of aeolian-
599 transported versus that of bedrock-derived clay minerals subjected to post-depositional mineral
600 alterations cannot be defined from the existing data.

601

602 **5.5 Relative timing of PM soil development**

603 Direct observations suggest that cryoturbation is a fundamental pedogenetic process in the
604 development of PM soil and continues today along with the ongoing accretion of the surficial aeolian
605 silt horizon Bw. The occurrence of seasonal soil freezing and lack of vegetation in the PM polygon
606 centers provide evidence that cryoturbation is active, destroying soil horizonation and obscuring
607 pedogenetic and chemical weathering signals. However, magnetic, and mineralogical data indicate
608 the occurrence of weathered Fe-(Ti) oxides such as (titano)maghemite, and the dominance of
609 smectite and kaolinite in the soil basal and topsoil layers, which enable us to conclude that mineral
610 alteration, and pedogenetic modifications of deposited aeolian dust and local erosional products are
611 ongoing processes within the PM soil profile, occurring in tandem with cryoturbation.

612 In the absence of absolute datings that can constrain temporally the processes driving the
613 production of PM soil, we hypothesized on its age based on the conclusions drawn from the
614 contributions of aeolian dust, and the impacts of cryoturbation. We tentatively ascribe the
615 deposition of the base colluvial layer and/or the *in-situ* fragmentation of the regolith's till boulders to
616 the most recent period of glacial activity on Mount Olympus. Based on the glacial record of the MK

617 and TZ cirques, the best candidates of periglacial activity that have likely resulted in the deposition of
618 outwash sand and gravels postdate the moraine stabilization phases at ~ 12.5 , 2.5, and 0.6 ka BP.

619 However, there is a 10-ka time span between the Holocene–Pleistocene boundary and the
620 late-Holocene glacial expansions on Mount Olympus. Accepting that PM soil formation began after
621 the moraine stabilization phase at ~ 12.5 ka BP that was common to MK and TZ cirques, its
622 production rate would be $\sim 3 \times 10^{-5}$ m yr⁻¹ assuming that soil erosion in the low-lying PM has been
623 minimal. This rate is considerably lower than respective soil production rates of Alpine and
624 Mediterranean soils formed over the last 10 ka (Egli et al., 2018; Figure 8). In contrast, by considering
625 a late-Holocene age and that the PM soil development postdates the ~ 2.5 ka BP moraine
626 stabilization phase, the soil production rate is $\sim 1 \times 10^{-4}$ m yr⁻¹ an estimate that is in better
627 agreement with the soil production rates presented by Egli et al. (2018) for both Alpine and
628 Mediterranean soils. Furthermore, a late-Holocene development of PM soil broadly agrees with soil
629 development patterns in diverse geomorphological environments in Crete (Kirsten and Heinrich,
630 2022). If this scenario is correct, then we can further hypothesize that development of the Bt horizon
631 could have lasted between ~ 2.5 and 1.0 ka BP, before a recorded phase of intense Sahara dust
632 accretion in Mediterranean that resulted from the combined action of an orbitally induced decrease
633 in solar insolation and of increased aridity over North Africa (Sabatier et al., 2020). This shift could
634 potentially explain the sharp textural boundary between the Bt and Bw horizons and the increasing
635 Sahara dust accretion on the upper Bw horizon. The hypothesized development of the Bw horizon
636 over the past 1 ka could have been disturbed by cryoturbation during the LIA (~ 0.6 ka BP) glacial
637 expansion in the MK and that continues until today. Ongoing work on Mount Olympus alpine critical
638 zone involves efforts to accurately date the MK and TZ scree interbedded layers and the PM soil
639 profile through Optically Stimulated Luminescence dating that is aided by the high concentrations of
640 quartz in the fine earth fraction, as well as additional geochemical analysis and estimates of the local
641 carbonate bedrock dissolution rates and its residual geochemical composition, in an overall attempt

642 to provide a new continuous record of postglacial alpine landscape evolution in the Mediterranean
643 periglacial zone.

644

645 **6 CONCLUSIONS**

646 In this study, we investigated the local processes that lead to the development of alpine soils on a
647 stable landform on Mount Olympus, considering its regional setting representative of Mediterranean
648 carbonate mountains that became gradually ice-free during the Pleistocene–Holocene transition but
649 that have also been affected by late-Holocene climatic shifts towards glacial and periglacial
650 conditions (Oliva et al., 2018). We discussed the relative contributions of erosion, aeolian dust
651 accretion, and post-depositional pedogenesis and mineral alteration by comparing colluvial sediment
652 layers interbedded in scree slopes with a soil B horizon developed on a regolith composed by slope
653 outwash deposits and fragmented till boulders along a 2km hillslope energy gradient with a
654 northeasterly orientation, which is the main direction of glacial cirque development on Mount
655 Olympus.

656 Overall, our results suggest that soils developed in stable landforms like the PM show signs of
657 weak pedogenesis and contain higher amounts of aeolian dust than locally eroded and chemically
658 weathered products. Aeolian dust from local and Saharan sources is accreted in alpine soils formed in
659 periglacial hummocky polygons of the PM and comprises ~30%–65% of the soil mass weight. This
660 interpretation matches those of several other studies on aeolian dust accretion in alpine soils (e.g.,
661 Gild et al., 2018; Kaüfmann, 2008; Munroe et al., 2015; Yang et al., 2016; Kirsten and Heinrich, 2022)
662 and suggests that aeolian dust is the primary parent soil material on Mount Olympus. The major
663 source of Sahara dust deposited on Mount Olympus is the Bodélé depression, which agrees with
664 observations of accreted dust in Crete (Pye, 1992).

665 In the low-erosional environment of the PM, mineral alteration and weak pedogenetic
666 modifications occur throughout the solum, but their signal is blurred by soil mixing due to ongoing

667 cryoturbation. A sharp textural boundary not visible in the field separates an upper weathered soil
668 Bw horizon from the lower Bt horizon, which is magnetically enhanced and enriched in smectite and
669 kaolinite. Radiogenic isotope systematics, mineralogy, and magnetic susceptibility value range
670 classify the Bw horizon as an aeolian silt layer that was likely formed during a late-Holocene shift of
671 regional atmospheric circulation that resulted in increased Sahara dust accretion in alpine
672 Mediterranean landscapes.

673

674

675

676

677 **REFERENCES**

- 678 Allard, J.L., Hughes, P.D., Woodward, J.C., Fink, D., Simon, K. & Wilcken, K.M. (2020) Late Pleistocene
679 glaciers in Greece: A new ³⁶Cl chronology. *Quaternary Science Reviews*, 245, 106528.
680 Available from: <https://doi.org/10.1016/j.quascirev.2020.106528>.
- 681 Amit, R., Enzel, Y. & Crouvi, O. (2020) Quaternary influx of proximal coarse-grained dust altered
682 circum-Mediterranean soil productivity and impacted early human culture: *Geology*, 49 (1),
683 61 – 65. Available from: <https://doi.org/10.1130/G47708.1>.
- 684 Anderson, S.P., Drever, J.I., Frost, C.D., Holden, P., 2000. Chemical weathering in the foreland of a
685 retreating glacier. *Geochim. Cosmochim. Acta* 64 (7), 1173– 1189.
- 686 Capo, R.C., Stewart, B.W. & Chadwick, O.A. (1998) Strontium isotopes as tracers of ecosystem
687 processes: theory and methods. *Geoderma*, 82, 197–225. Available from:
688 [https://doi.org/10.1016/S0016-7061\(97\)00102-X](https://doi.org/10.1016/S0016-7061(97)00102-X)
- 689 Castorina, F., Magganas, A., Masi, U. & Kyriakopoulos, K. (2020) Geochemical and Sr-Nd isotopic
690 evidence for petrogenesis and geodynamic setting of Lower-Middle Triassic volcanogenic
691 rocks from central Greece: Implications for the Neotethyan Pindos ocean. *Mineralogy &*
692 *Petrology*, 114, 39–56. Available from: <https://doi.org/10.1007/s00710-019-00687-7>.
- 693 Conroy, J.L., Overpeck, J.T., Cole, J.E., Liu, K.B., Wang, D. Ducea, M.D. 2013. Dust and temperature
694 influences on glaciofluvial sediment deposition in southwestern Tibet during the last
695 millennium. *Global and Planetary Change*, 107, 132-144.
696 <https://doi.org/10.1016/j.gloplacha.2013.04.009>.
- 697 Dearing, J., Hay, K., Baban, S., Huddleston, A., Wellington, E. & Loveland, P. (1996) Magnetic
698 susceptibility of soil: an evaluation of conflicting theories using a national data set.
699 *Geophysical Journal International*, 127, 728–734.
- 700 Dobiński, W., 2005. Permafrost of the Carpathian and Balkan Mountains, Eastern and Southeastern
701 Europe. *Permafrost and Periglacial Process*, 16, 395–398.
- 702 Drewnik, M., Skiba, M., Szymański, W. & Żyła, M. (2014) Mineral composition vs. soil forming
703 processes in loess soils — A case study from Kraków (Southern Poland), *Catena*, 119, 166 -
704 173. Available from: <http://dx.doi.org/10.1016/j.catena.2014.02.012>
- 705 Ducea, M. N., Barla, A., Stoica, A. M., Panaiotu, C. & Petrescu, L. (2020) Temporal-geochemical
706 evolution of the Persani volcanic field, eastern Transylvanian Basin (Romania): Implications
707 for slab rollback beneath the SE Carpathians. *Tectonics*, 39e2019TC005802. Available from:
708 <https://doi.org/10.1029/2019TC005802>
- 709 Dunlop, D.J. & Özdemir, Ö. (1997) *Rock Magnetism: Fundamentals and Frontiers*. Cambridge
710 University Press, Cambridge, New York.
- 711 Durn, G., Ottner, F. & Slovenec, D. (1999) Mineralogical and geochemical indicators of the
712 polygenetic nature of terra rossa in Istria, Croatia. *Geoderma*, 91, 125–150.
- 713 Durn, G. (2003) Terra rossa in the Mediterranean region: parent materials, composition and origin.
714 *Geolgika Croatia*, 56, 83 – 100.
- 715 Egli, M., Mirabella, A. & Fitze, P. (2003) Formation rates of smectites derived from two Holocene
716 chronosequences in the Swiss Alps. *Geoderma*, 117, 81–98.
- 717 Egli, M., Wernli, M., Burga, C., Kneisel, C., Mavris, C., Valboa, G., Mirabella, A., Plotze, M. &
718 Haerberli, W. (2011) Fast but spatially scattered smectite-formation in the proglacial area
719 Morteratsch: an evaluation using GIS. *Geoderma*, 164, 11–21.
- 720 Egli, M., Dahms, D. & Norton, K. (2014) Soil formation rates on silicate parent material in alpine
721 environments: Different approaches—different results? *Geoderma*, 213, 320 – 333.

- 722 Egli, M. & Poulénard, J. (2016) Soils of Mountainous Landscapes. In International Encyclopedia of
723 Geography: People, the Earth, Environment and Technology (eds D. Richardson, N. Castree,
724 M.F. Goodchild, A. Kobayashi, W. Liu and R.A. Marston). Available from:
725 <https://doi.org/10.1002/9781118786352.wbieg0197>
- 726 Egli, M., Hunt, A.G., Dahms, D., Raab, G., Derungs, C., Raimondi, S. & Yu, F. (2018) Prediction of Soil
727 Formation as a Function of Age Using the Percolation Theory Approach. *Frontiers in*
728 *Environmental Science*, 6, 108. Available from: <https://doi.org/10.3389/fenvs.2018.00108>.
- 729 Erel, Y. & Torrent, J. (2010) Contribution of Saharan dust to Mediterranean soils assessed by
730 sequential extraction and Pb and Sr isotopes. *Chemical Geology*, 275, 19–25. Available from:
731 <https://doi.org/10.1016/j.chemgeo.2010.04.007>.
- 732 Frank, A.B., Frei, R., Triantaphyllou, M., Vassilakis, E., Kristiansen, K. & Frei K.M. (2021) Isotopic range
733 of bioavailable strontium on the Peloponnese peninsula, Greece: A multi-proxy approach.
734 *Science of the Total Environment*, 774, 145181, Available from:
735 <https://doi.org/10.1016/j.scitotenv.2021.145181>.
- 736 Gaillardet, J., Calmels, D., Romero-Mujalli, G., Zakharova, E., Hartmann, J. 2019. Global climate
737 control on carbonate weathering intensity. *Chemical Geology*, 527, 118762.
738 <https://doi.org/10.1016/j.chemgeo.2018.05.009>.
- 739 Garzanti, E., Andò, S. & Vezzoli, G. (2009) Grain-size dependence of sediment composition and
740 environmental bias in provenance studies. *Earth and Planetary Science Letters*, 277, 3–4,
741 422–432. Available from: <https://doi.org/10.1016/j.epsl.2008.11.007>.
- 742 Gild, C., Geitner, C. & Sanders, D. (2018) Discovery of a landscape-wide drape of late-glacial aeolian
743 silt in the western Northern Calcareous Alps (Austria): First results and implications.
744 *Geomorphology* 301, 39–52. Available from:
745 <https://doi.org/10.1016/j.geomorph.2017.10.025>.
- 746 Goudie, A.S. & Middleton, N.J. (2001) Saharan dust storms: nature and consequences. *Earth Science*
747 *Reviews*, 56, 179 - 204.
- 748 Grousset, F.E. & Biscaye, P.E. (2005) Tracing dust sources and transport patterns using Sr, Nd and Pb
749 isotopes. *Chemical Geology* 222, 149–167. Available from:
750 <https://doi.org/10.1016/j.chemgeo.2005.05.006>.
- 751 Haeberli, W., Hallet, B., Arenson, L., Elconin, R., Humlum, O., Kääb, A., Kaufmann, V., Ladanyi, B.,
752 Matsuoka, N., Springman, S. & Vonder Mühl, D. (2006) Permafrost creep and rock glacier
753 dynamics. *Permafrost and Periglacial Processes*, 17, 189–214. Available from:
754 <http://doi.org/10.1002/ppp.561>.
- 755 Jewell, A.M., Drake, N., Crocker, A.J., Bakker, N.L., Kunkelova, T., Bristow, C.S., Cooper, M.J., Milton,
756 J.A., Breeze, P.S. & Wilson, P.A. (2021) Three North African dust source areas and their
757 geochemical fingerprint. *Earth Planetary Science Letters*, 554, 116645. Available from:
758 <https://doi.org/10.1016/j.epsl.2020.116645>.
- 759 Jordanova, N., Jordanova, D., Qingsong, L., Pengxiang, H., Petrov, P. & Petrovský, E. (2013) Soil
760 formation and mineralogy of a Rhodic Luvisol — insights from magnetic and geochemical
761 studies. *Global and Planetary Change*, 110, 397–413.
- 762 Jordanova, D., Georgieva, B., Jordanova, N., Guyodo, Y. & Lagroix, F. (2022) Holocene
763 palaeoenvironmental conditions in NE Bulgaria uncovered by mineral magnetic and
764 paleomagnetic records of an alluvial soil, *Quaternary International*, 631, 47–58.
765 <https://doi.org/10.1016/j.quaint.2022.06.009>.
- 766 Kantiranis N. (2001) Calcination study of the crystalline limestone from Agios Panteleimonas, Florina,
767 Greece. PhD Thesis, School of Geology, Aristotle University of Thessaloniki, 196p.

- 768 Küfmann, C. (2008) Are cambisols in alpine karst Autochthonous or eolian in origin? *Arctic Antarctic*
769 *and Alpine Research*, 40, 506–518.
- 770 Kirsten, F. & Heinrich, J. (2022) Soil-sediment-configurations on slopes of Central and Western Crete
771 (Greece) and their implications for late Holocene morphodynamics and pedogenesis – A
772 conceptual approach, *Catena*, 214, 106238, 0341-8162. Available from:
773 <https://doi.org/10.1016/j.catena.2022.106238>.
- 774 Krklec, K., Braucher, R., Perica, D. & Domínguez-Villar, D. (2022) Long-term denudation rate of karstic
775 North Dalmatian Plain (Croatia) calculated from ³⁶Cl cosmogenic nuclides. *Geomorphology*,
776 413, 108358. <https://doi.org/10.1016/j.geomorph.2022.108358>.
- 777 Kuhlemann, J., Rohling, E., Krumrei, I., Kubik, P., Ivy-Ochs, S. & Kucera, M. (2008) Regional synthesis
778 of Mediterranean atmospheric circulation during the last glacial maximum. *Science*, 321
779 (5894), 1338 – 1340.
- 780 Kurtz, A.C., Derry, L.A. & Chadwick, O.A. (2001) Accretion of Asian dust to Hawaiian soils; isotopic,
781 elemental, and mineral mass balances. *Geochimica Cosmochimica Acta*, 65, 1971–1983.
- 782 Lawrence, C.R., Reynolds, R.L., Ketterer, M.E. & Neff, J.C. (2013) Aeolian controls of soil geochemistry
783 and weathering fluxes in high-elevation ecosystems of the Rocky Mountains, Colorado.
784 *Geochimica Cosmochimica Acta*, 107, 27–46.
- 785 Lehmkuhl, F., Nett, J.J., Pötter, S., Schulte, P., Sprafke, T., Jary, Z., Antoine, P., Wacha, L., Wolf, D.,
786 Zerboni, A., Hošek, J., Marković, S.B., Obrecht, I., Sümegi, P., Veres, D., Zeeden, C., Boemke, B.,
787 Schaubert, V., Viehweger, J. & Hambach, U. (2020) Loess landscapes of Europe - mapping,
788 geomorphology, and zonal differentiation. *Earth Science Reviews*, 215, 103496. Available
789 from: <https://doi.org/10.1016/j.earscirev.2020.103496>.
- 790 Lutterotti L., Bortolotti M., Ischia G., Lonardelli I. & Wenk H.R. (2007) Rietveld texture analysis from
791 diffraction images. *Zeitschrift für Kristallographie*, 26, 125-130.
- 792 Maher, B.A. (2011) The magnetic properties of Quaternary aeolian dusts and sediments, and their
793 palaeoclimatic significance. *Aeolian Research*, 3, 87–144.
- 794 Marmureanu, L., Marin, C.A., Andrei, S., Antonescu, B., Ene, D., Boldeanu, M., Vasilescu, J., Vitelaru,
795 C., Cadar, O. & Levei, E. (2019) Orange snow: a Saharan dust intrusion over Romania during
796 winter conditions. *Remote Sensing*, 11, 2466. Available from:
797 <https://doi.org/10.3390/rs11212466>.
- 798 Mattsson, J.O. & Nihlén, T. (1996) The transport of Saharan dust to southern Europe: a scenario.
799 *Journal of Arid Environments*, 32 (2), 111–119. Available from:
800 <https://doi.org/10.1006/jare.1996.0011>.
- 801 Macleod, D.A. (1980) The origin of the red Mediterranean soils in Epirus. Greece. *European Journal of*
802 *Soil Science*, 31 (1), 125–136.
- 803 Merino, E. & Banerjee, A. (2008) Terra rossa genesis, implications for karst, and eolian dust: a
804 geodynamic thread. *Journal of Geology*, 116, 62 – 75.
- 805 Moskowitz, B.M., Reynolds, R.L., Goldstein, H.L., Berquó, T.S., Kokaly, R.F. & Bristow, C.S. (2016) Iron
806 oxide minerals in dust-source sediments from the Bodélé Depression, Chad: Implications for
807 radiative properties and Fe bioavailability of dust plumes from the Sahara. *Aeolian Research*,
808 22, 93-106, Available from: <https://doi.org/10.1016/j.aeolia.2016.07.001>.
- 809 Muhs, D.R. & Benedict, J.B. (2006) Eolian additions to late Quaternary alpine soils, Indian Peaks
810 Wilderness Area, Colorado Front Range. *Arctic Antarctic and Alpine Research*, 38, 120–130.

- 811 Munroe, J.S., Attwood, E.C., O’Keefe, S.S. & Quackenbush, P.J. (2015) Eolian deposition in the alpine
812 zone of the Uinta Mountains, Utah, USA. *Catena* 124, 119–129.
- 813 Munroe, J.S., Norris, E.D., Carling, G.T., Beard, B.L., Satkoski, A.M. & Liu, L. (2019) Isotope
814 fingerprinting reveals western North American sources of modern dust in the Uinta
815 Mountains, Utah, USA. *Aeolian Research*, 38, 39-47. Available from:
816 <https://doi.org/10.1016/j.aeolia.2019.03.005>.
- 817 Oliva, M., Žebre, M., Guglielmin, M., Hughes, P.D., Çiner, A., Vieira, G., Bodin, X., Andrés, N., Colucci,
818 R.R., García-Hernández, C., Mora, C., Nofre, J., Palacios, D., Pérez-Alberti, A., Ribolini, A., Ruiz-
819 Fernández, J., Sarıkaya, M.A., Serrano, E., Urdea, P., Valcárcel, M., Woodward, J.C. & Yıldırım,
820 C. (2018) Permafrost conditions in the Mediterranean region since the Last Glaciation, *Earth
821 Science Reviews*, 185, 397-436, Available from:
822 <https://doi.org/10.1016/j.earscirev.2018.06.018>.
- 823 Ott, R. F., Gallen, S. F. & Helman, D. (2023) Erosion and weathering in carbonate regions reveal
824 climatic and tectonic drivers of carbonate landscape evolution, EGUsphere [preprint],
825 Available from: <https://doi.org/10.5194/egusphere-2022-1376>.
- 826 Pye, K. (1992) Aeolian dust transport and deposition over Crete and adjacent parts of the
827 Mediterranean sea. *Earth Surface Processes and Landforms*, 17, 271–288. Available from:
828 <https://doi.org/10.1002/esp.3290170306>.
- 829 Rellini, I., Trombino, L., Firpo, M. & Rossi, P.M. (2009) Extending westward the loess basin between
830 the Alps and the Mediterranean region: micromorphological and mineralogical evidence
831 from the northern slope of the Ligurian Alps, Northern Italy. *Geografia Fisica Dinamica
832 Quaternaria*, 32, 103–116.
- 833 Remoundaki, E., Bourliva, A., Kokkalis, P., Mamouri, R.E., Papayannis, A., Grigoratos, T., Samara, C.,
834 Tsezos, M. (2011) PM10 composition during an intense Saharan dust transport event over
835 Athens (Greece). *Science of The Total Environment*, 409, 20,4361-4372. Available from:
836 <https://doi.org/10.1016/j.scitotenv.2011.06.026>.
- 837 Rodriguez-Navarro, C., di Lorenzo, F. & Elert, K. (2018) Mineralogy and physicochemical features of
838 Saharan dust wet deposited in the Iberian Peninsula during an extreme red rain event,
839 *Atmospheric Chemistry and Physics* 18, 10089–10122. Available from:
840 <https://doi.org/10.5194/acp-18-10089-2018>.
- 841 Runnels, C. & van Andel, T.J. (2003) The early stone age of the nomos of Preveza: landscape and
842 settlement. In *Landscape Archaeology in Southern Epirus, Greece, Vol. I*, Wiseman J, Zachos K
843 (eds). *Hesperia Supplement*, 32, 47–13.
- 844 Sabatier, P., Nicolle, M., Piot, C., Colin, C., Debret, M., Swingedouw, D., Perrette, Y., Bellingery, M.S.,
845 Chazeau, B., Develle, A.L., Leblanc, M., Skonieczny, C., Copard, Y., Reyss, J.L., Malet, E.,
846 Jouffroy-Bapicot, I., Kelner, M., Poulenard, J., Didier, J., Arnaud, F. & Vannièrè, B. (2020) Past
847 African dust inputs in the western Mediterranean area controlled by the complex interaction
848 between the Intertropical Convergence Zone, the North Atlantic Oscillation, and total solar
849 irradiance. *Climate of the Past*. 16 283–298. Available from: [https://doi.org/10.5194/cp-16-
850 283-2020](https://doi.org/10.5194/cp-16-283-2020).
- 851 Sanders, D., Ostermann, M. & Kramers, J. (2010) Meteoric diagenesis of Quaternary carbonate rocky
852 talus slope successions (Northern Calcareous Alps, Austria). *Facies*, 56, 27–46.
- 853 Šarić, K., Cvetković, V., Romer, R.L., Christofides, G. & Koroneos, A (2009) Granitoids associated with
854 East Vardar ophiolites (Serbia, F.Y.R. of Macedonia and northern Greece): Origin, evolution
855 and geodynamic significance inferred from major and trace element data and Sr–Nd–Pb

856 isotopes. *Lithos*, 108, 1–4, 131–150. Available from:
857 <https://doi.org/10.1016/j.lithos.2008.06.001>.

858 Scheuvens, D., Schütz, L., Kandler, K., Ebert, M. & Weinbruch, S. (2013) Bulk composition of northern
859 African dust and its source sediments – a compilation. *Earth Science Reviews*, 116, 170–194.
860 Available from: <https://doi.org/10.1016/j.earscirev.2012.08.005>

861 Shalev, N., Lazar, B., Halicz, L., Stein, M., Gavrieli, I., Sandler, A. & Segal, I. (2013) Strontium Isotope
862 Fractionation in Soils and Pedogenic Processes. *Procedia Earth and Planetary Science*, 7, 790–
863 793. Available from: <https://doi.org/10.1016/j.proeps.2013.03.074>.

864 Statham, I. (1976) A scree slope rockfall model. *Earth Surface Processes*, 1, 43–62.

865 Stuut, J.B., Smalley, I. & O’Hara-Dhand, K. (2009) Aeolian dust in Europe: African sources and
866 European deposits. *Quaternary International*, 198 (1–2), 234–245. Available from:
867 <https://doi.org/10.1016/j.quaint.2008.10.007>

868 Styllas, M.N., Schimmelpfennig, I., Ghilardi, M. & Benedetti, L. (2016) Geomorphologic and
869 paleoclimatic evidence of Holocene glaciation on Mount Olympus, Greece. *The Holocene*, 26
870 (5), 709–721.

871 Styllas, M. N., Schimmelpfennig, I., Benedetti, L., Ghilardi, M., Aumaître, G., Bourlès, D. &
872 Keddadouche, K. (2018) Late-glacial and Holocene history of the northeast Mediterranean
873 mountain glaciers – New insights from in situ-produced ³⁶Cl-based cosmic ray exposure dating
874 of paleo-glacier deposits on Mount Olympus, Greece, *Quaternary Science Reviews*, 193, 244–
875 265, Available from: <https://doi.org/10.1016/j.quascirev.2018.06.020,2018>

876 Styllas, M.N. & Kaskaoutis, D.G. (2018) Relationship between winter orographic precipitation with
877 synoptic and large-scale atmospheric circulation: the case of Mount Olympus, Greece.
878 *Bulletin of Geological Society of Greece*, 52, 45 – 70.

879 Styllas M. (2020) Tracing a late Holocene glacial climatic signal from source to sink under intensifying
880 human erosion of eastern Mediterranean landscapes. *Mediterranean Geoscience Reviews* 2,
881 91–101. Available from: <https://doi.org/10.1007/s42990-020-00031-8>.

882 Varga, G., Cserhati, C., Kovacs, J. & Szalai, Z. (2016) Saharan dust deposition in the Carpathian Basin
883 and its possible effects on interglacial soil formation. *Aeolian Research*, 22. Available from:
884 <https://doi.org/10.1016/j.aeolia.2016.05.004>.

885 Weldeab, S., Emeis, K-C., Hemleben, C. & Siebel, W. (2002) Provenance of lithogenic surface
886 sediments and pathways of riverine suspended matter in the Eastern Mediterranean Sea:
887 evidence from 143Nd/144Nd and 87Sr/86Sr ratios, *Chemical Geology*, 186, 1–2, 139–149,
888 [https://doi.org/10.1016/S0009-2541\(01\)00415-6](https://doi.org/10.1016/S0009-2541(01)00415-6).

889 Wu, L., Krijgsman, W., Liu, J., Li, C., Wang, R. & Xiao, W. (2020) CFLab: A MATLAB GUI program for
890 decomposing sediment grain size distribution using Weibull functions. *Sedimentary Geology*,
891 398, 105590. Available from: <https://doi.org/10.1016/j.sedgeo.2020.105590>.

892 Yaalon, D.H. (1997) Soils in the Mediterranean region: what makes them different? *Catena*, 28, 157–
893 169. Available from: [https://doi.org/10.1016/S0341-8162\(96\)00035-5](https://doi.org/10.1016/S0341-8162(96)00035-5).

894 Yang, F., Zhang, G.L., Yang, F. & Yang, R.M. (2016) Pedogenetic interpretations of particle-size
895 distribution curves for an alpine environment. *Geoderma*, 282, 9–15

896

897

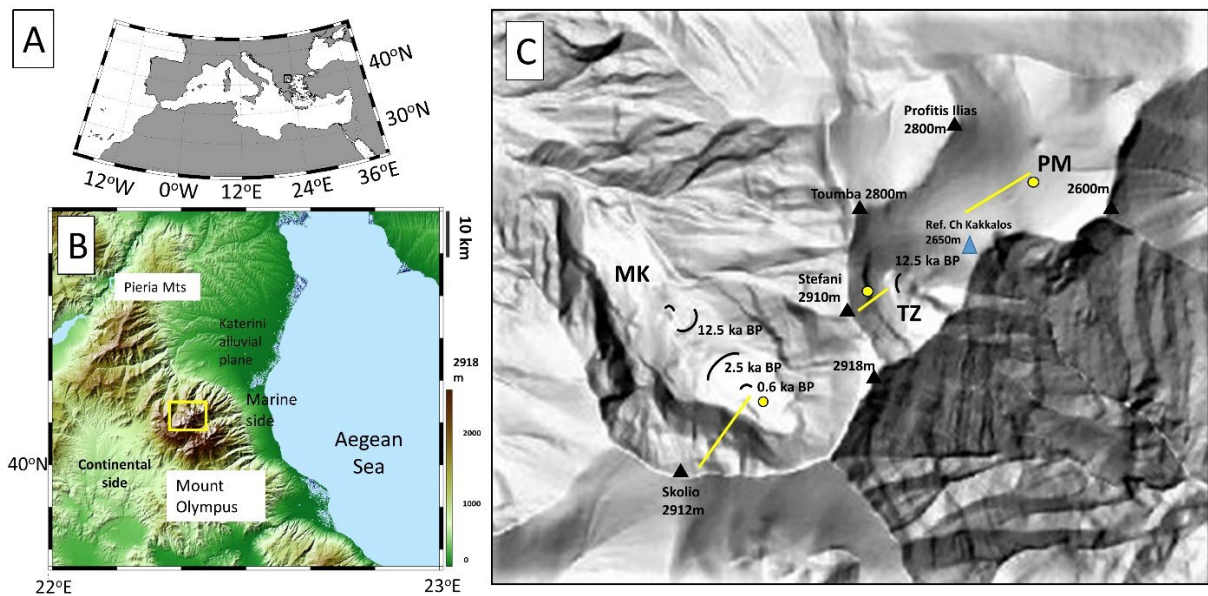
898

899

900 **FIGURES**

901 **Figure 1.** (A) General setting of the study area within the Mediterranean basin. (B) Mount Olympus
902 alpine domain that is considered in the study (yellow box), with the two respective piedmonts on the
903 marine and continental sides, the adjacent Pieria Mountains and Katerini alluvial plane (SRTM 90
904 DEM Model). (C) The highest cirques and plateau of Mount Olympus with the respective locations of
905 dated moraines (black curved lines from Styllas et al., 2018), the sampling locations considered in this
906 study (yellow circles) and the geomorphological transects described in Figure 2 (yellow lines). MK:
907 Megala Kazania cirque, TZ: Throne of Zeus cirque, PM: Plateau of Muses.

908

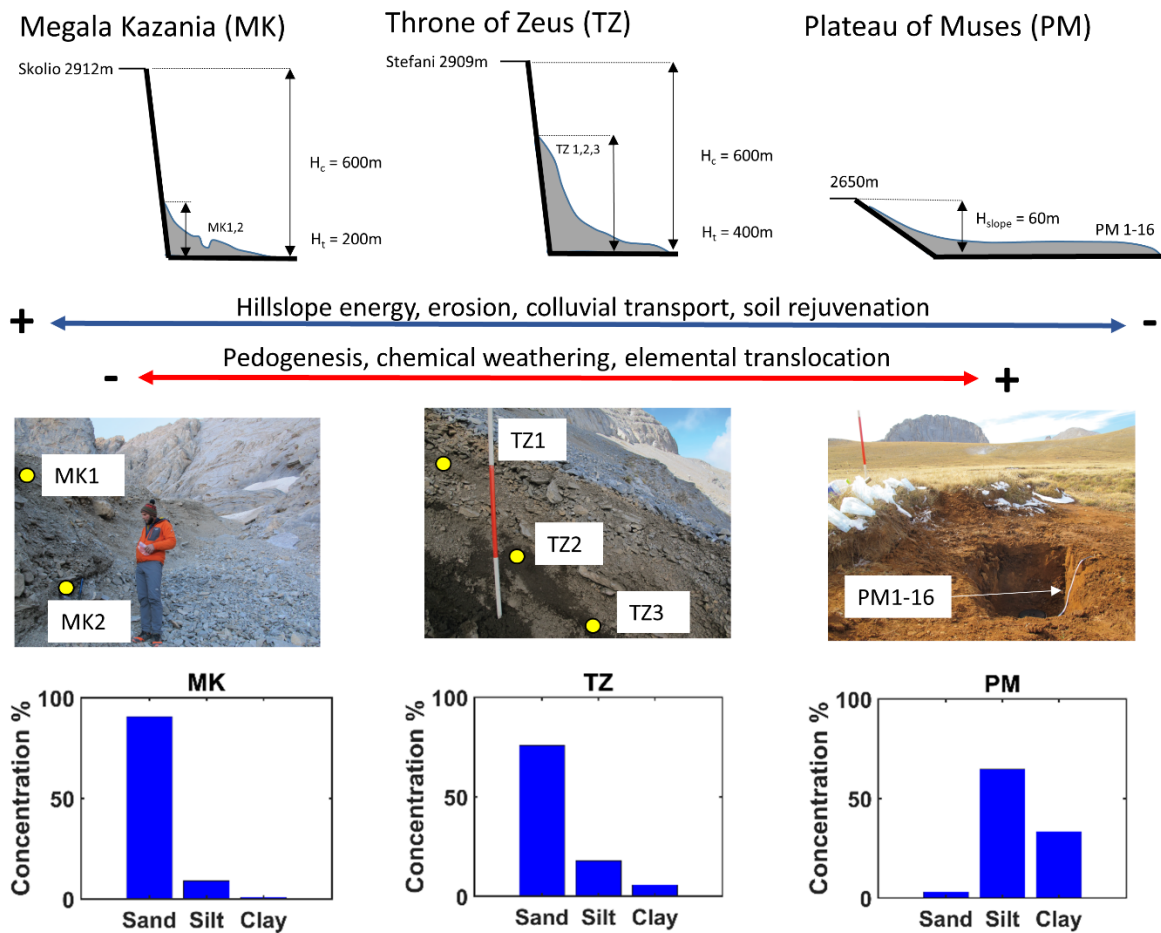


909

910

911

912 **Figure 2.** Conceptual diagram of the study, with the sampling sites and their morphological profiles,
 913 shown in Figure 1c as yellow lines, and with their respective textural characteristics that resulted
 914 from the grain size analysis. The respective heights of the rock cliffs (H_c) and talus slopes (H_t) are
 915 shown. The soil samples from the stratified scree clast free horizons in MK cirque are located behind
 916 the Little Ice Age moraine (left upper panel, photo, and diagram). The stratified scree slope under the
 917 rock wall of Stefani (2910m) in the TZ cirque, with the respective locations of the clast free soil
 918 samples (center panel, photo, and diagram) and the soil profile in the PM (right panel, photo, and
 919 diagram).



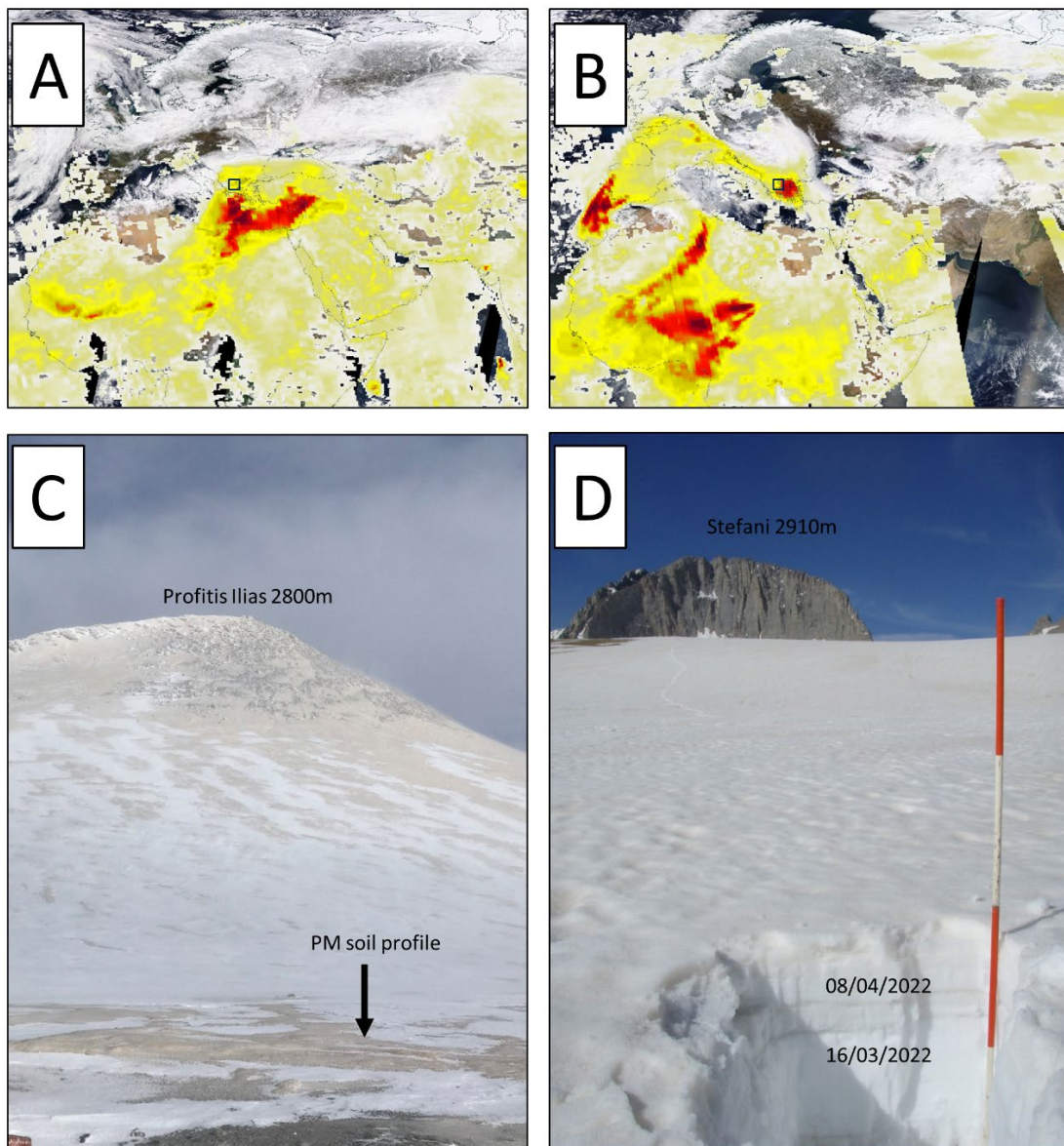
920

921

922

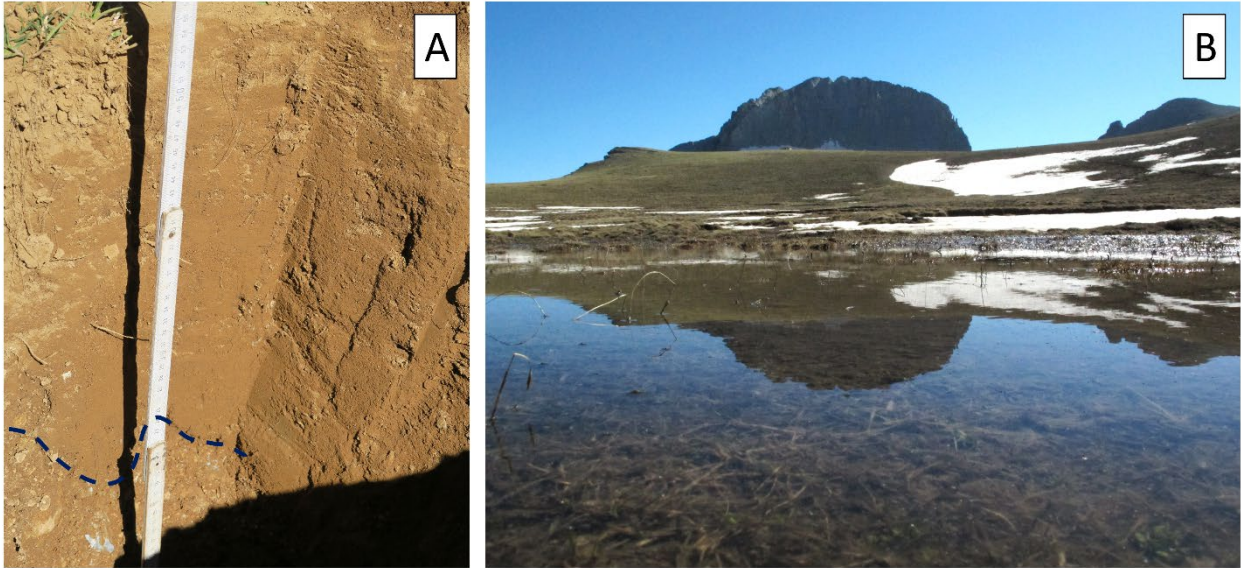
923 **Figure 3.** Synoptic maps and direct observations of two Sahara dust episodes on Mount Olympus
924 alpine critical zone (black rectangle). (A). Aerosol Optical Depth (AOD) during March 22, 2018, and (B)
925 and March 16, 2022, showing the trajectory of dust plume from Sahara Desert, and their impacts on
926 the snowpack of the Plateau of Muses (C and D). The PM soil profile was excavated under the black
927 arrow (C), whereas the snow pit (D) with two successive Sahara dust transport episodes in the spring
928 of 2022, has also been excavated on top of the PM soil profile excavated pit. The NASA SUOMI/NNP
929 Aerosol Optical Depth composition product was downloaded from the NASA EOSDIS Worldview
930 platform (worldview.earthdata.nasa.gov).

931



932

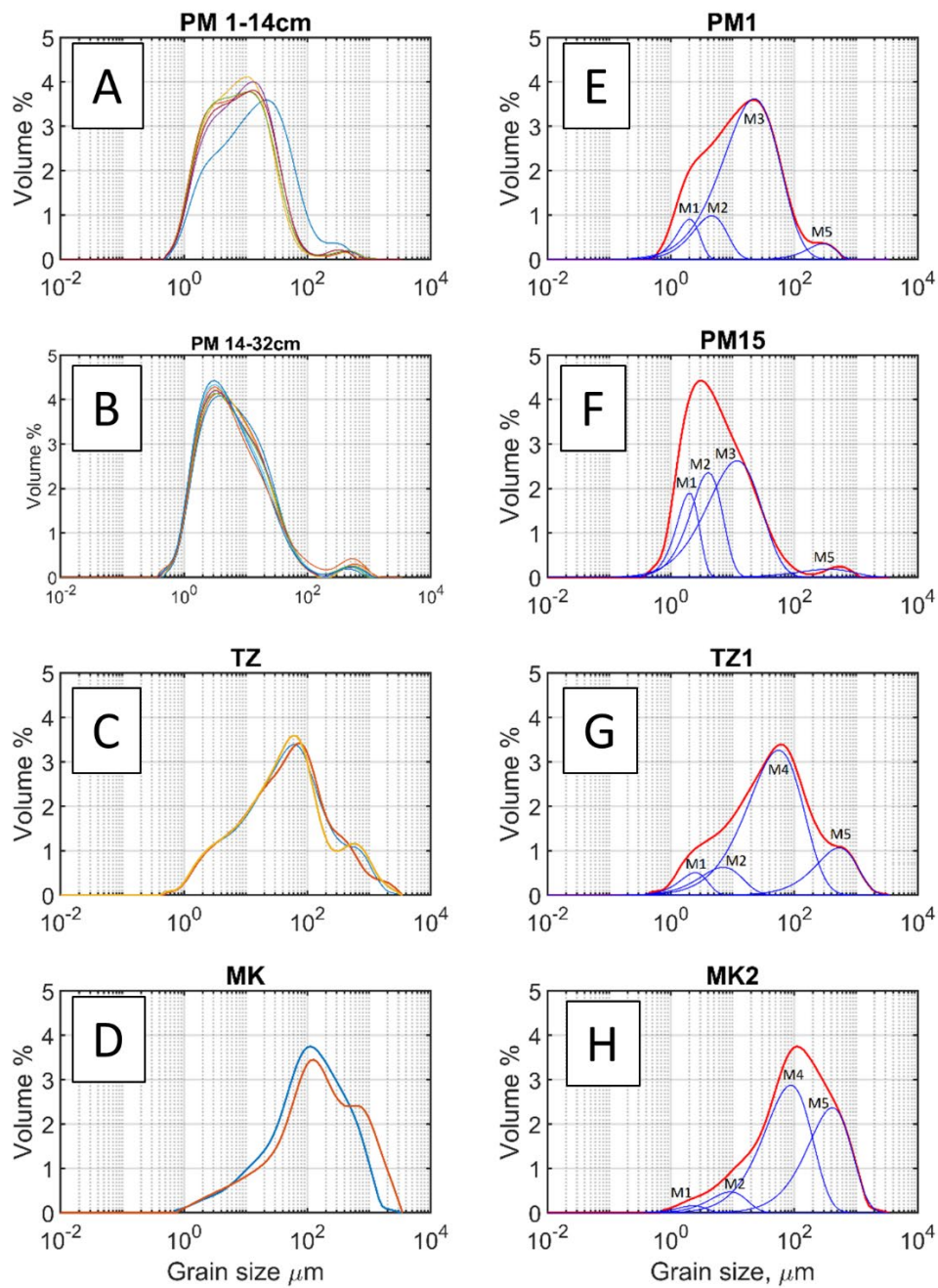
933 **Figure 4.** Evidence of soil disturbance on the Plateau of Muses under past and present-day climatic
934 conditions. (A) An irregular gravel layer (blue dashed line) between colluvial gravel and the overlying
935 soil resulting from cryoturbation. (B) Early summer season ongoing freeze of the soil surface layer
936 and subsequent waterlogging (photo taken on June 2012).



937

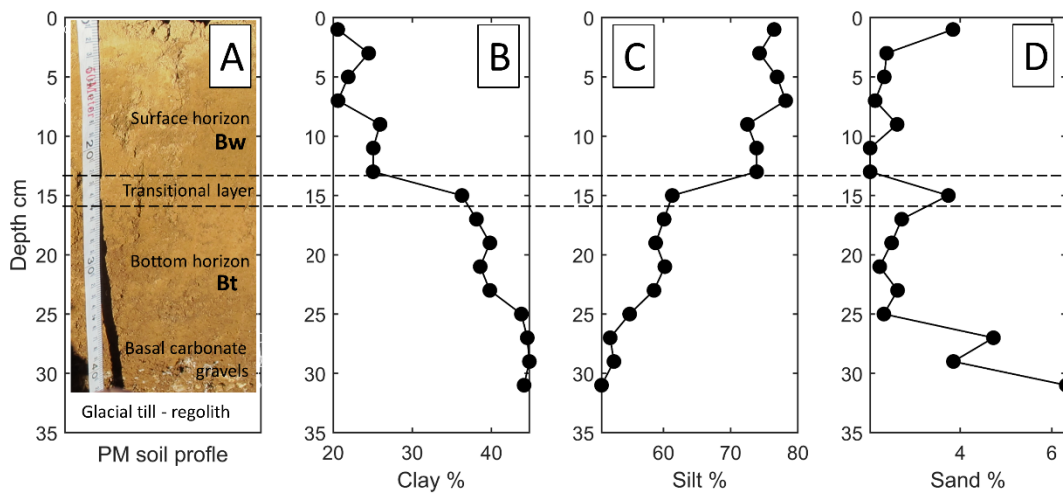
938

939 **Figure 5.** Cumulative grain size distributions of the soil samples from MK, TZ and PM Bw and Bt
 940 horizons (A, B, C and D). Surface sample PM1 (A, blue line) shows a distinct grain size distribution
 941 from the PM soil upper layer. Subplots E, F, G and H: Results of the CFLab fitting algorithm with the
 942 respective grain size distributions (GSD) and extracted grain size modes M1 to M5 (blue curves) of
 943 the soil samples PM1, PM15, TZ1 and MK2, represented as distinct sub-populations.



944

945 **Figure 6.** The PM soil profile along with the depth variations main textural classes. A transition layer
 946 between 14 and 16 cm of depth marks a substantial decrease in clay and increase in silt contents and
 947 a change in the dry soil color. For clarity reasons, it is noted that the direct depth measurement of
 948 the PM soil begins at 10 cm along the measurement tape, explaining the discrepancy between the
 949 actual and the illustrated depth. The photo was taken one day after the profile excavation, when the
 950 upper part had partly dried out.

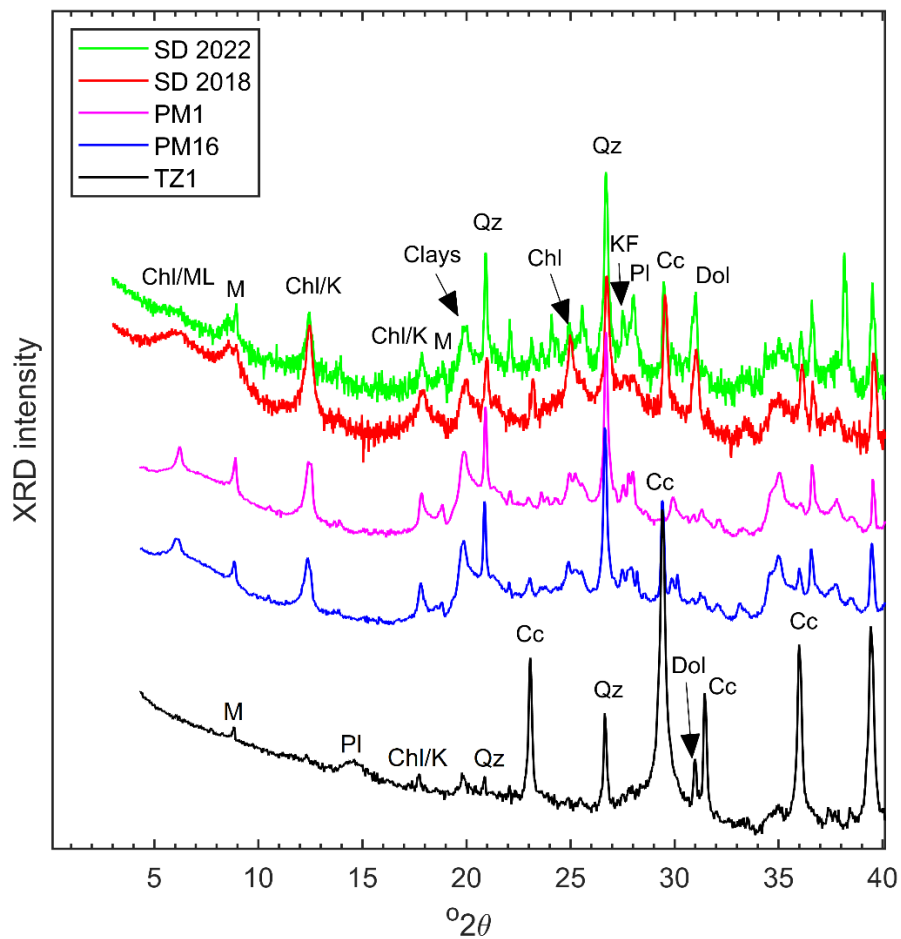


951

952

953

954 **Figure 7.** X-ray diffraction patterns of soil samples PM1, PM15, TZ1 and MK2. Soils within the
 955 hillslope high energy scree deposits are composed primarily of calcite. In contrast PM soil samples
 956 contain quartz, clays, feldspars, and mica. (M: mica, Chl/M: Chlorite and mixed layer clays, likely
 957 smectite, Chl/K: chlorite and likely kaolinite, K: K feldspar, Qz: quartz, Pl: plagioclase feldspars, Cc:
 958 calcite, Dol: Dolomite).



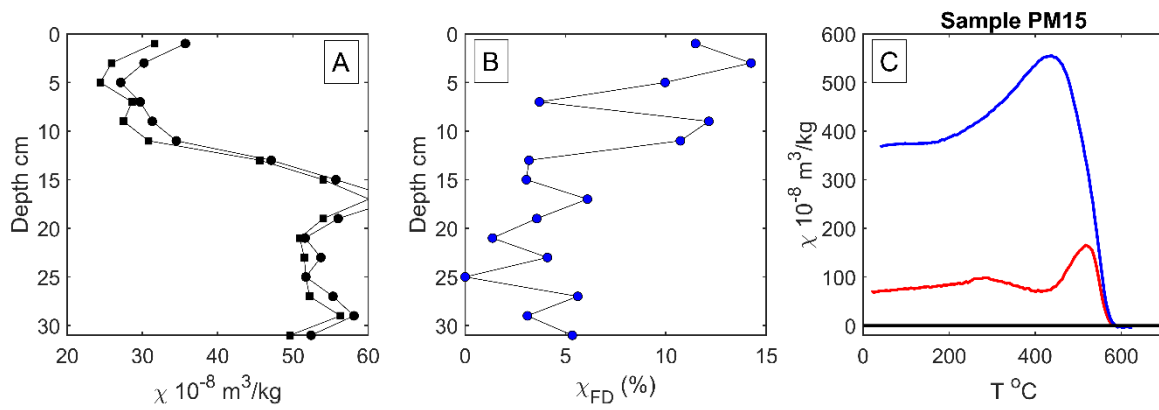
959

960

961

962

963 **Figure 8.** Depth variations of low and high frequency (A) and frequency dependent magnetic
964 susceptibility (B) and (C) thermomagnetic analysis results of sample PM15 (red heating curve, blue
965 cooling curve).



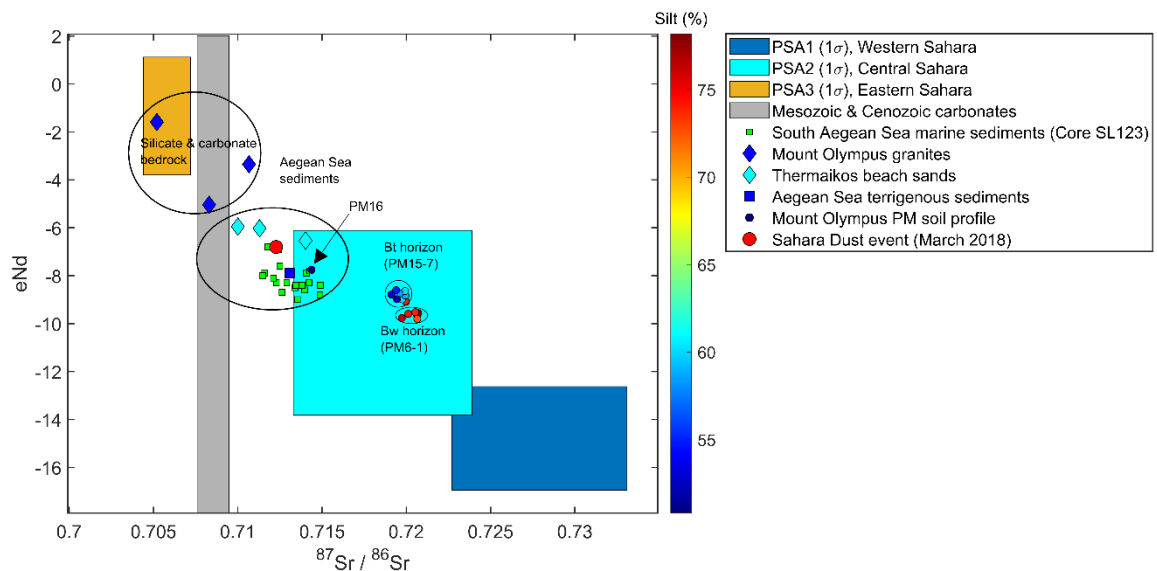
966

967

968

969 **Figure 9.** Plot of $^{87}\text{Sr}/^{86}\text{Sr}$ against ϵ_{Nd} values of the PM soil samples with respective values of Mesozoic
 970 and Cretaceous carbonates (Franck et al., 2021), Mount Olympus granites (located on the continental
 971 west sides of the massif (Šarić et al., 2009, Castorina et al., 2020), Aegean Sea terrigenous and coastal
 972 sediments (Weldeab et al., 2002) and South Aegean marine sediments from Core SL 123 (Ehrmann et
 973 al., 2007), along with the three main North African dust source areas (PSA, Jewell et al., 2021). The
 974 isotopic enrichment trend for the PM soil samples towards crustal more radiogenic values occurs
 975 with a 25% increase in silt contents (colorbar) from the base to the surface of PM soil profile,
 976 suggesting the influence of external aeolian dust.

977



978

979

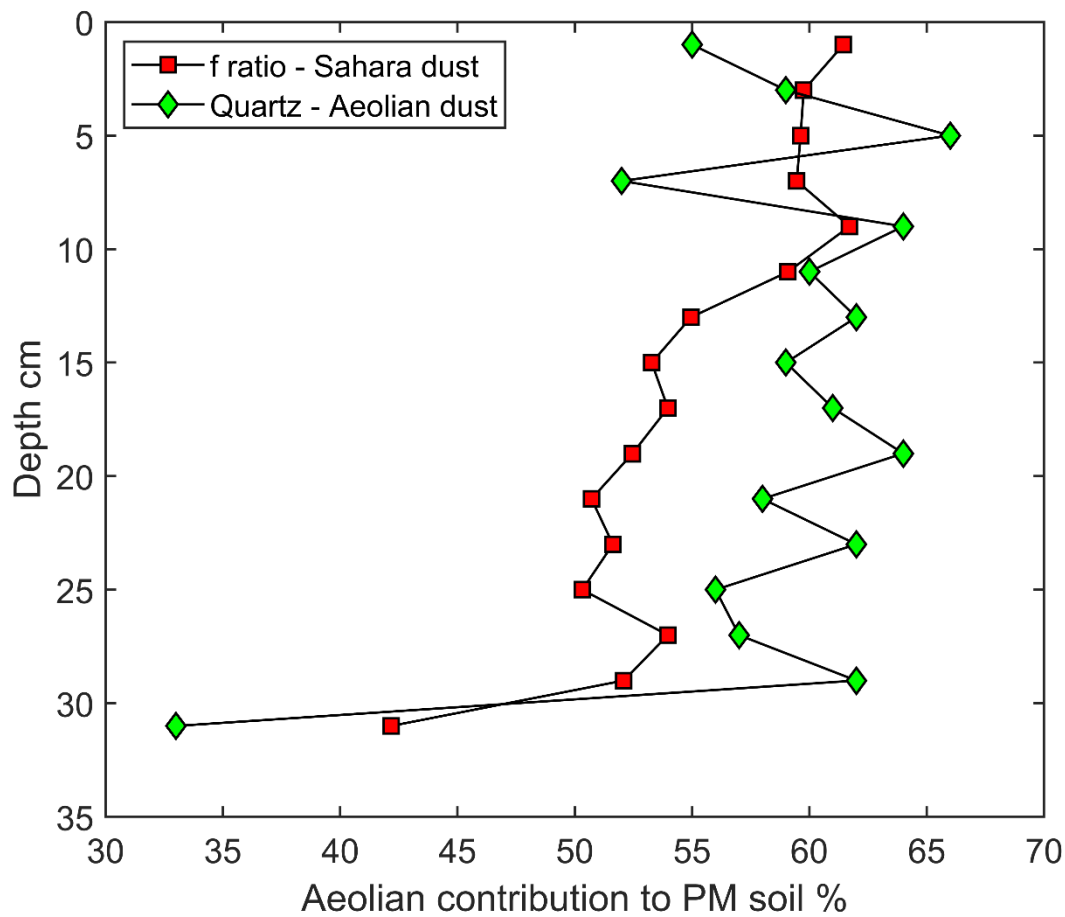
980

981

982

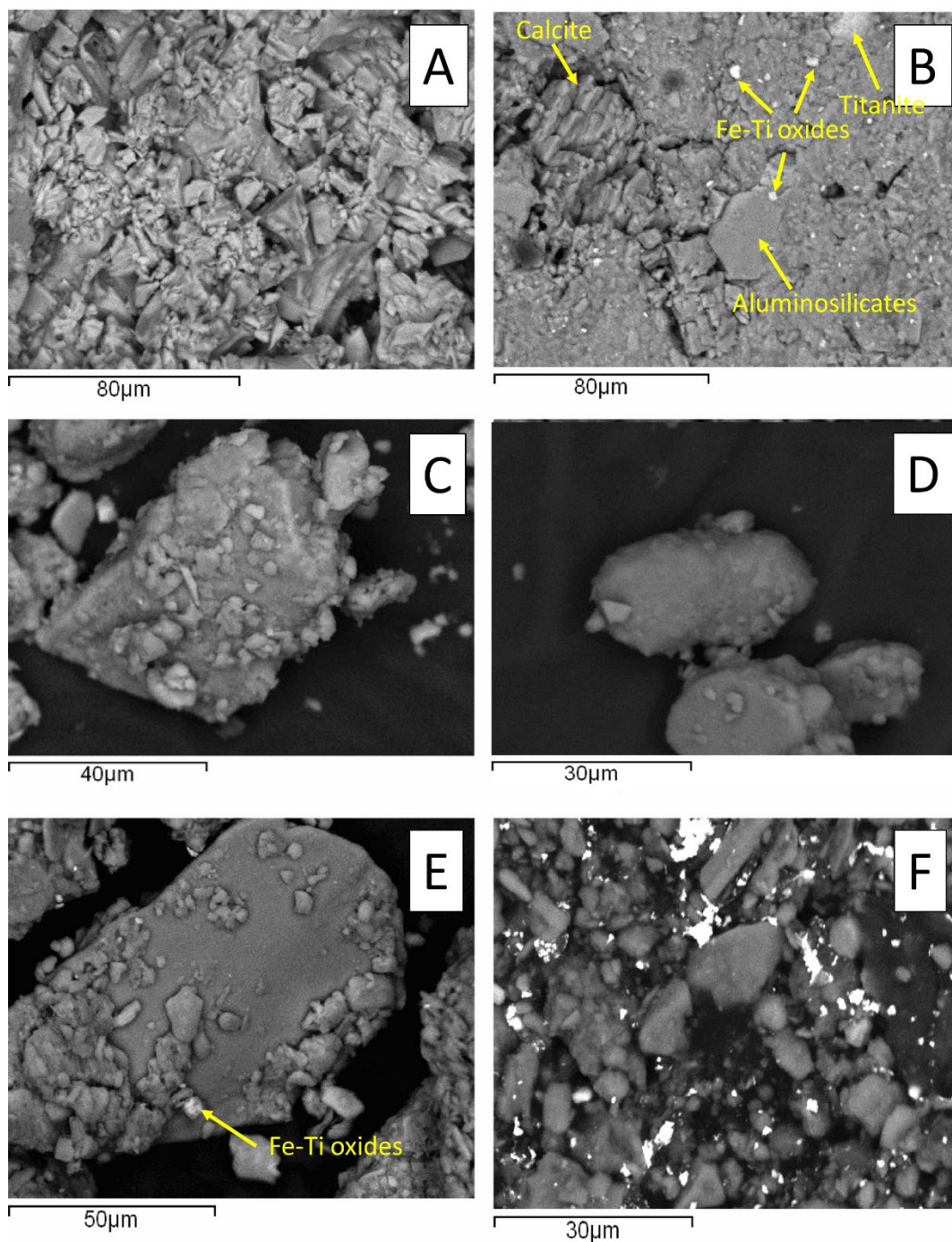
983

984 **FIGURE 10.** Estimates of the relative contributions of aeolian dust accretion to PM soil as calculated
985 by mineralogical, and isotopic proxies.



986
987
988
989
990
991
992
993

994 **FIGURE 11.** SEM backscatter images from selected samples of PM loess profile. (A) Calcite grains
 995 from basal sample PM 16. (B) Mixed phase of aluminosilicates with calcite, titanomagnetite and
 996 titanite from basal sample PM 16. (C) K-feldspar. (D) Quartz grain with rounded edges as a result of
 997 long-range aeolian transport. (E) Surface sample PM1 aggregate of aluminosilicates and Fe-Ti oxides.
 998 (F) Quartz grains of variable shapes and grain sizes from sample PM3 along with Fe-Ti oxides.



999

1000 **Table 1.** Physical characteristics of the soil samples retrieved from the interbedded colluvial soils of
 1001 the Megala Kazania (MK) and Throne of Zeus (TZ) scree slopes and from the alpine soil formed on the
 1002 Plateau of Muses (PM).

Sample id	Depth (cm)	Munsell color (dry)	Clay (%) ($<2\mu\text{m}$)	Fine Silt (%) ($3.5\text{-}5\mu\text{m}$)	Silt (%) ($14\text{-}30\mu\text{m}$)	Fine sand (%) ($65\text{-}110\mu\text{m}$)	Coarse sand (%) ($300\text{-}800\mu\text{m}$)
MK1	30	5Y 6/1	1.7	6.6	0.0	39.8	51.9
MK2	250	5Y 6/1	0.0	11.4	0.0	47.5	41.1
TZ1	50	2.5Y 5/4	5.3	10.0	0.0	67.9	16.8
TZ2	150	10YR 3/4	6.0	25.2	0.0	43.5	25.3
TZ3	120	10YR 3/4	5.8	18.2	0.0	56.9	19.1
PM1	0-2	7.5YR 3/6	7.8	12.7	76.5	0.0	3.0
PM2	2-4	7.5YR 3/6	9.8	14.7	74.5	0.0	1.0
PM3	4-6	7.5YR 3/6	8.5	13.4	76.9	0.0	1.2
PM4	6-8	7.5YR 3/6	8.0	12.6	78.2	0.0	1.2
PM5	8-10	7.5YR 3/6	9.8	16.1	72.5	0.0	1.6
PM6	10-12	7.5YR 2/4	9.3	15.7	73.8	0.0	1.2
PM7	12-14	7.5YR 3/6	9.3	15.7	73.8	0.0	1.2
PM8	14-16	10YR 3/4	13.0	23.3	61.3	0.0	2.4
PM9	16-18	10YR 3/4	13.8	24.2	60.1	0.0	1.9
PM10	18-20	10YR 2/4	14.5	25.2	58.8	0.0	1.5
PM11	20-22	10YR 3/4	14.0	24.5	60.2	0.0	1.3
PM12	22-24	10YR 3/6	14.6	25.1	58.6	0.0	1.7
PM13	24-26	10YR 3/6	16.3	27.5	55.0	0.0	1.2

PM14	26-28	10YR 3/4	16.0	28.5	52.1	0.0	3.4
PM15	28-30	10YR 4/6	16.2	28.6	52.6	0.0	2.6
PM16	30-32	2.5YR 5/6	15.6	28.5	50.8	0.0	5.1

1003

1004

1005 **Table 2.** Weight percent (wt %) mineralogical semi quantitative composition of the PM soil, along
 1006 with the clay mineralogy of surface and base samples PM1 and PM15.

Sample id	Qtz	Chl_CC	Plag	KF	Mica	Amph	Cc	Clay mineralogy (<2µm) Sm / Kaol / Chl / Ill
PM1	55	21	14	3	7	0	0	Smectite: 45%, Kaolinite: 35%, Chlorite: 10%, Illite:10%
PM2	59	26	6	1	8	0	0	
PM3	66	21	4	2	7	0	0	
PM4	52	31	7	3	7	0	0	
PM5	64	22	7	0	7	0	0	
PM6	60	24	7	2	7	0	0	
PM7	62	20	4	6	8	0	0	
PM8	59	24	7	3	7	0	0	
PM9	61	24	7	3	5	0	0	
PM10	64	22	8	1	5	0	0	
PM11	58	28	4	3	7	0	0	
PM12	62	22	7	2	7	0	0	
PM13	56	25	5	1	7	6	0	
PM14	57	28	2	7	6	0	0	
PM15	62	24	6	4	4	0	0	Smectite: 65%, Kaolinite: 25%, Chlorite: 5%, Illite:5%
PM16	33	12	1	2	4	0	48	

1007

1008

1009 **Table 3.** Radiogenic isotope results for the PM soil profile and the 2018 Sahara dust (SD) samples.

1010 ϵ ND values were calculated

Sample id	$^{87}\text{Sr}/^{86}\text{Sr}$		$^{143}\text{Nd}/^{144}\text{Nd}$		ϵ_{ND}
	$^{87}\text{Sr}/^{86}\text{Sr}$	std err (%)	$^{143}\text{Nd}/^{144}\text{Nd}$	std. err. (%)	
NBS 987 Sr standard	0.7102500	0.0008	-	-	
La Jolla Nd standard	-	-	0.5118500	0.0006	
PM1	0.7197322	0.0008	0.5121292	0.0004	-9.77
PM2	0.7201146	0.0026	0.5121383	0.0006	-9.60
PM3	0.7205816	0.0009	0.5121390	0.0006	-9.58
PM4	0.7207105	0.0010	0.5121399	0.0007	-9.56
PM5	0.7206530	0.0029	0.5121278	0.0009	-9.80
PM6	0.7205393	0.0007	0.5121419	0.0005	-9.52
PM7	0.7199828	0.0008	0.5121641	0.0005	-9.09
PM8	0.7196993	0.0009	0.5121731	0.0006	-8.91
PM9	0.7197594	0.0008	0.5121694	0.0005	-8.98
PM10	0.7199571	0.0007	0.5121775	0.0004	-8.82
PM11	0.7199244	0.0009	0.5121869	0.0006	-8.64
PM12	0.7196162	0.0008	0.5121820	0.0006	-8.74
PM13	0.7193930	0.0008	0.5121890	0.0006	-8.60
PM14	0.7194477	0.0009	0.5121694	0.0005	-8.98
PM15	0.7191162	0.0011	0.5121795	0.0004	-8.79
PM16	0.7143748	0.0016	0.5122328	0.0005	-7.75
SD 2018	0.7122721	0.0009	0.5122813	0.0006	-6.80

1011